Title	Studies on Novel Catalysts for Methane and Toluene Combustion by using Ceria-Zirconia Based Solid Solutions as a Promoter
Author(s)	Jeong, Minchan
Citation	大阪大学, 2018, 博士論文
Version Type	VoR
URL	https://doi.org/10.18910/69551
rights	
Note	

Doctoral Dissertation

Studies on Novel Catalysts for Methane and Toluene Combustion by using Ceria–Zirconia Based Solid Solutions as a Promoter

（セリア–ジルコニア系固溶体を助触媒として用いた新規なメタンおよびトルエン燃焼触媒に関する研究）

Minchan Jeong

January 2018

Division of Applied Chemistry
Graduate School of Engineering
Osaka University

Studies on Novel Catalysts for Methane and Toluene Combustion by using Ceria–Zirconia Based Solid Solutions as a Promoter

（セリア-ジルコニア系固溶体を助触媒として用いた新規なメタンおよびトルエン燃焼触媒に関する研究）

2018

Minchan Jeong

Division of Applied Chemistry
Graduate School of Engineering
Osaka University

Preface

The work of this thesis has been carried out under the supervision of Professor Dr. Nobuhito Imanaka at Divison of Applied Chemistry, Graduate School of Engineering, Osaka University.

The object of this thesis is to develop novel environmental catalysts for complete oxidation of methane and toluene at moderate temperatures.

The author wishes that the findings and the knowledge obtained in this work will provide useful suggestions and information for further development and design of novel environmental catalysts and that the materials would contribute to more practical applications.

Minchan Jeong

Division of Applied Chemistry

Graduate School of Engineering

Osaka University

2-1 Yamadaoka, Suita,

Osaka 565-0871,

Japan

January 2018

Contents

Chapter 1

Complete Combustion of Methane using Novel CeO_2–ZrO_2 Based Catalysts

Chapter 2

Effect of Conductivities in CeO_2–ZrO_2 Based Promoters on Catalytic Activities

Chapter 3

Complete Combustion of Toluene using Novel CeO_2–ZrO_2 Based Catalysts

General Introduction

During the past several decades, rapid development of science and technology makes our life convenient and comfortable. On the other hand, global concerns for environment (e.g. global warming and air pollution) have increased due to various kinds of chemical substances. Methane (CH_4) is the second most damaging greenhouse effect gas generated by human activities after carbon dioxide, and its warming effect is approximately 20 times higher than that of carbon dioxide [1]. Methane is the main component of natural gas, widely used as a fuel resource for engines and power stations; however, the principal drawback related to natural gas usage is the emission of unburned methane. In order to reduce global warming, it is important to suppress methane emission into the atmosphere [2].

Meanwhile, toluene (C_7H_8) is also urgently required for removal from the atmosphere. Toluene has been widely used as an organic solvent for paint thinners, printing inks, floor wax, adhesives, and antiseptic, because it can dissolve various organic compounds and is easily produced from petroleum fractions [3]. However, toluene brings harmful effects for human health and induces photochemical smog formation. Even at low concentration of toluene, released from consumer products, such as floor wax and wall paint, it may cause sick building syndrome [4]. In order to protect our health, it is necessary to remove toluene vaporized into indoor air.

In general, several technologies for methane and toluene removal have been proposed, such as direct combustion method [5], heat accumulation combustion method [6], activated-carbon adsorption method [7], and catalytic combustion method [8]. Among them, catalytic combustion is an ideal technology, because combustion of methane and toluene into harmless water vapor and carbon dioxide can be realized at low operating cost and relatively low temperatures, leading to minimal negative side effects such as NO_x production [8,9]. The conventional combustion catalysts have been eagerly studied on noble metal based catalysts, such as Pd/γ-Al_2O_3 and Pt/γ-Al_2O_3. These catalysts needed to be heated at 800 °C [10] and 240 °C [11] to completely oxidize methane and toluene, respectively.

For the effective combustion of methane and toluene at moderate temperatures, it is considered to be difficult to oxidize them by using only the adsorbed oxygen on the activator from the atmospheric air. Thus, promoters that can supply oxygen from the crystal lattice to the activator were focused. The diagram of oxygen supply from the promoter is shown in Figure G-1. Oxygen species is supplied to the activator from the interior of the lattice (oxygen release), involved with the migration of oxide ion through the lattice of the promoter (ionic conduction). Gaseous oxygen is stored as lattice oxide ion within the promoter (oxygen storage). Due to these oxygen release and storage processes of the promoter, the catalytic oxidation of organic compounds is facilitated. For the catalyst with the promoter, the redox property is a key factor, because a redox reaction is required to store gaseous oxygen as lattice oxide ions and to subsequently release active oxygen species. In addition, it is considered that the oxide-ion conductivity also affects the oxygen release and storage abilities.

Ceria (CeO_2) has been well-known as a promoter due to its oxygen release and storage abilities by means of facile Ce^{4+}/Ce^{3+} redox cycle [12,13]. Since the partial substitution of Ce^{4+} with Zr^{4+} in the CeO_2 lattice enhances the oxygen release and storage abilities, the ceria–zirconia (CeO_2–ZrO_2) solid solution has been employed as exhaust catalysts [14]. Furthermore, it is reported that the complete oxidations for noble metal supported on CeO_2–ZrO_2 were realized at 550 °C (Pd/CeO_2–ZrO_2) [15] and 140 °C (Pt/CeO_2–ZrO_2/γ-Al_2O_3) [16] for methane and toluene, respectively, which were relatively lower than the Pd/γ-Al_2O_3 (800 °C) and Pt/γ-Al_2O_3 (240 °C) cases. However, further lower operating temperatures are required for methane and toluene combustion. Since CeO_2–ZrO_2 promoter was employed for a high-temperature exhaust gas, it is necessary to enhance oxygen release and storage abilities of promoters at moderate temperatures.

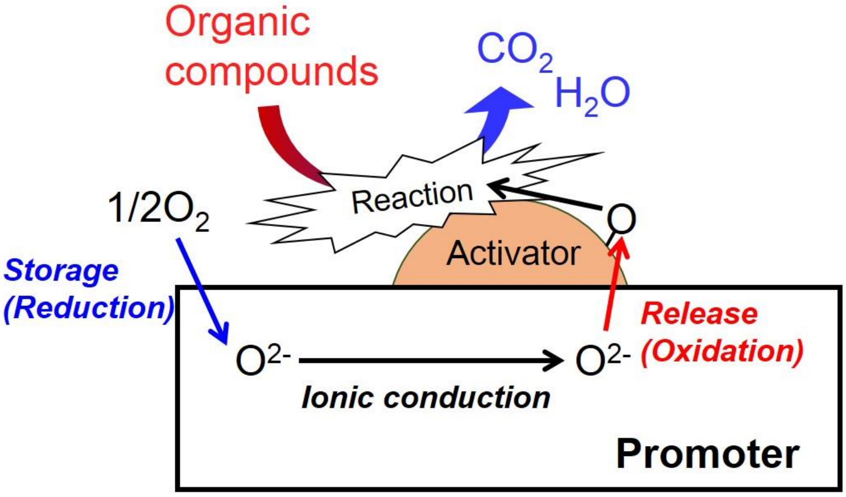

Figure G-1. Diagram of possible oxygen supply for the oxidation reaction on activator loaded on promoter.

The aim of this thesis is to develop novel environmental catalysts capable of completely oxidizing methane and toluene into carbon dioxide and steam at the temperature as low as possible. To this end, novel CeO_2–ZrO_2 based promoters were prepared to enhance oxygen release and storage abilities. In addition, the effect of the oxide-ionic-conducting and redox properties on the oxygen release and storage abilities and the catalytic activity was investigated.

This thesis consists of the following three chapters.

In Chapter 1, iron oxide (Fe_2O_3) or nickel oxide (NiO) were doped into the CeO_2–ZrO_2 lattice to improve the oxygen release and storage abilities, because the introduction of ions with low valency forms oxygen vacancy for oxide ion migration pathway. In addition, two valence states ($Fe^{3+/2+}$, $Ni^{3+/2+}$) are expected to facilitate the redox properties due to valence changes of $Fe^{3+/2+}$ or $Ni^{3+/2+}$. From these concepts, PdO/CeO_2–ZrO_2–Fe_2O_3/γ-Al_2O_3 and PdO/CeO_2–ZrO_2–NiO/γ-Al_2O_3 catalysts were synthesized, and the catalytic activities for methane combustion were investigated.

In Chapter 2, the effect of the oxide-ion conductivity and redox property on the oxygen release and storage abilities and the catalytic activity for CeO_2–ZrO_2 based catalysts was investigated.

In Chapter 3, in order to oxidize toluene at temperatures as low as possible, novel Pt/CeO_2–ZrO_2–NiO/γ-Al_2O_3 catalyst was prepared by using CeO_2–ZrO_2–NiO as a promoter, and the catalytic activity was investigated.

List of publications

1. Effect of introducing Fe_2O_3 into CeO_2-ZrO_2 on oxygen release properties and catalytic methane combustion over PdO/CeO_2-ZrO_2-Fe_2O_3/γ-Al_2O_3 catalysts

   Minchan Jeong, Naoyoshi Nunotani, Naoki Moriyama, Nobuhito Imanaka

   Catalysis Science & Technology, 2017, 7, 1986~1990.

2. High methane combustion activity of PdO/CeO_2-ZrO_2-NiO/γ-Al_2O_3 catalysts

   Minchan Jeong, Naoyoshi Nunotani, Naoki Moriyama, Nobuhito Imanaka

   Journal of Asian Ceramic Societies, 2016, 4, 259~262.

3. Relationship between the conductivities of CeO_2-ZrO_2-MO_x (M = Bi, Ca, Sn, Ni, Fe) solid solution and catalytic activities during methane oxidation

   Minchan Jeong, Naoyoshi Nunotani, Nobuhito Imanaka

   Bulletin of the Chemical Society of Japan, in press.

4. Introduction of NiO in Pt/CeO_2-ZrO_2/γ-Al_2O_3 catalysts for removing toluene in indoor air

   Minchan Jeong, Naoyoshi Nunotani, Naoki Moriyama, Nobuhito Imanaka

   Materials Letters, 2017, 208, 43~45.

Chapter 1

Complete Combustion of Methane using Novel CeO_2–ZrO_2 Based Catalysts

1.1 Introduction

Recently, it is reported that the introduction of bismuth oxide (Bi_2O_3) into the CeO_2–ZrO_2 lattice effectively improved the oxygen release and storage abilities [17-20], because the migration of active oxygen was facilitated via the oxygen vacancy, generated by the partial substitution of Bi^{3+} ions having lower valency than Ce^{4+} and Zr^{4+} due to the charge compensation. Furthermore, the combination of PdO, CeO_2–ZrO_2–Bi_2O_3, and γ-Al_2O_3 was effective in the methane oxidation. Among the PdO/CeO_2–ZrO_2–Bi_2O_3/γ-Al_2O_3 catalysts, the 11.6wt%PdO/15wt%$Ce_{0.62}Zr_{0.17}Bi_{0.21}O_{1.89}$/$\gamma$-$Al_2O_3$ catalyst exhibited the highest activity, and methane was completely oxidized at 320 °C [21].

In Chapter 1, Fe_2O_3 and NiO were focused as the substitute for Bi_2O_3 into CeO_2–ZrO_2 to facilitate methane oxidation at moderate temperatures. It is anticipated that oxygen vacancies are formed by introducing lower vacancy $Ni^{3+/2+}$ and $Fe^{3+/2+}$ ions into the CeO_2–ZrO_2 lattice, which is similar to the CeO_2–ZrO_2–Bi_2O_3 case. In addition, since Fe and Ni ions exist in two valence states, +3 and +2, further enhancement in oxygen release and storage abilities is expected due to the redox of $Ni^{3+/2+}$ and $Fe^{3+/2+}$ ions. Accordingly, I developed novel PdO/CeO_2–ZrO_2–MO_x/γ-Al_2O_3 (M = Fe, Ni) catalysts, and their catalytic activities for methane combustion were investigated.

1.2 Experimental Procedure

The $Ce_{0.8(1-x)}Zr_{0.2(1-x)}Fe_xO_{2.0-\delta}/\gamma\text{-}Al_2O_3$ (CZFe(x)/Al_2O_3) and $Ce_{0.8(1-x)}Zr_{0.2(1-x)}Ni_xO_{2.0-\delta}/\gamma\text{-}Al_2O_3$ (CZNi(x)/Al_2O_3) samples were synthesized via the conventional wet coprecipitation method. Before preparation, commercial $\gamma\text{-}Al_2O_3$ (AxSorb AB, Nippon Light Metal) was ground in an agate mortar, and then mechanically pulverized by a ball-milling apparatus (Pulverisette 7, FRITSCH GmbH) at a rotation speed of 300 rpm for 2 h. Aqueous solutions of 1.0 $mol\cdot L^{-1}$ $Ce(NO_3)_3$, 0.1 $mol\cdot L^{-1}$ $ZrO(NO_3)_2$, and 0.1 $mol\cdot L^{-1}$ $Fe(NO_3)_3$ (or $Ni(NO_3)_2$) were mixed with 15 mL of 3 $mol\cdot L^{-1}$ HNO_3 in stoichiometric amounts. The solution was then impregnated on the $\gamma\text{-}Al_2O_3$ powder, with the CZFe(x) and CZNi(x) content adjusted to 10–25wt%. The mixture was stirred at room temperature for 30 min, and the pH of the solution was adjusted to 11 by the dropwise addition of aqueous ammonia (6%). After stirring for 12 h at room temperature, the resulting precipitate was collected by filtration, washed several times with deionized water, and then dried at 80 °C for 6 h. Subsequently, these samples were heated at 500 °C for 1 h under ambient air atmosphere. For comparison, 11.3wt% PdO/16wt%$Ce_{0.68}Zr_{0.17}Bi_{0.15}O_{2-\delta}/\gamma\text{-}Al_2O_3$ catalyst was also prepared by the same coprecipitation and impregnation methods using 0.5 $mol\cdot L^{-1}$ $Bi(NO_3)_3$ instead of 0.1 $mol\cdot L^{-1}$ $Fe(NO_3)_3$.

Supported palladium catalysts were prepared by the impregnation of $Pd(NO_2)_2(NH_3)_2$ solution (Tanaka Kikinzoku Kogyo) into the CZFe(x)/Al_2O_3 and CZNi(x)/Al_2O_3 samples. Subsequently, the catalysts were dried at 80 °C for 12 h and then calcined at 400 °C for 4 h. The amounts of PdO were adjusted to 8.0–13.6wt%.

X-ray powder diffraction (XRD; SmartLab, Rigaku) patterns were measured with Cu Kα radiation (40 kV, 30 mA) in the 2θ range from 10° to 70° with a step size of 0.02° and a scan speed of $2°\cdot min^{-1}$. Brunauer–Emmett–Teller (BET) specific surface area was measured by nitrogen adsorption at −196 °C (TriStar 3000, Shimadzu). Temperature-programmed reduction (TPR) measurement was carried out under a flow of 5 vol% hydrogen–argon (50 $mL\cdot min^{-1}$) at a heating rate of 5 °C·min^{-1} up to 500 °C (BELCAT-B, MicroTracBEL). Following the TPR experiments, the catalyst was outgassed under a helium flow, and then, oxygen storage capacity (OSC) values were determined using the pulse-injection method at 427 °C. Pluses of oxygen (0.3 mL) were injected into the helium flow (50 mL·min^{-1}) passing through the catalyst until the breakthrough point was achieved. The OSC value was evaluated as the uptake of oxygen from the oxygen pulse (BELCAT-B, MicroTracBEL).

The methane oxidation activity was tested in a conventional fixed-bed flow reactor consisting of a quartz glass tube (diameter = 10 mm) with a feed gas mixture of 1 vol% methane–air at a rate of 33.4 mL·min^{-1} over 0.1 g of catalyst. Here, the space velocity was 20,000 L·kg^{-1}·h^{-1}. The catalysts were pretreated at 200 °C for 2 h under argon flow (20 mL·min^{-1}) prior to the catalytic activity tests. The catalytic activity was evaluated in terms of the approximately-constant methane conversion at each temperature maintained for over an hour. The gas composition after the reaction was analyzed using gas chromatography with Molecular Sieve 5A column and thermal conductivity detection (GC-8AIT, Shimadzu).

1.3 Results and Discussion

1.3.1 PdO/CeO_2–ZrO_2–Fe_2O_3/γ-Al_2O_3 catalyst

Figure 1.1 shows the XRD patterns of the 11.3wt%PdO/20wt%$Ce_{0.8(1-x)}Zr_{0.2(1-x)}Fe_xO_{2.0-\delta}$/γ-$Al_2O_3$ (11.3wt%PdO/20wt%CZFe(x)/Al_2O_3) (x = 0, 0.1, 0.15, 0.2) catalysts. The patterns clearly indicated the formation of a crystalline phase indexed by a cubic fluorite-type, PdO, and a γ-Al_2O_3 phase, and crystalline impurities were not confirmed.

The measured compositions and BET specific surface areas of the 11.3wt%PdO/20wt%CZFe(x)/Al_2O_3 (x = 0, 0.1, 0.15, 0.2) catalysts are tabulated in Table 1.1. The measured compositions are in good agreement with the stoichiometric values within the experimental error. The BET specific surface areas of 11.3wt%PdO/20wt%CZFe(x)/Al_2O_3 were lower than that of 11.3wt%PdO/20wt%CZ/Al_2O_3, likely due to the lower melting point of Fe_2O_3 (1566 °C (decomposition)) [22] compared to CeO_2 (2445 °C) [23] and ZrO_2 (2710 °C) [23].

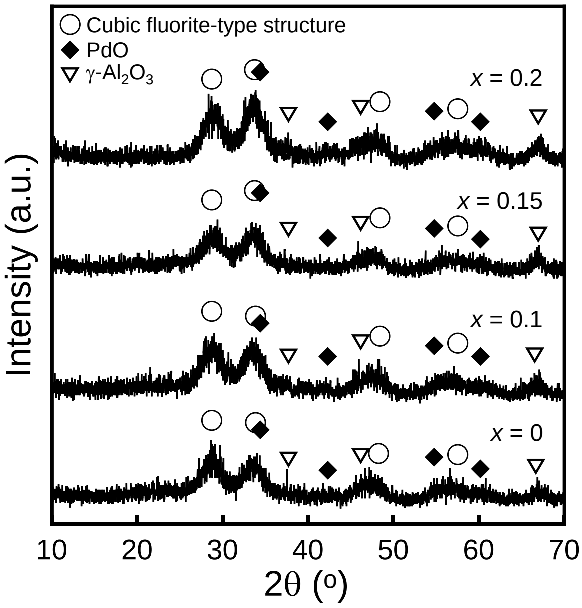

Figure 1.1. XRD patterns of the 11.3wt%PdO/20wt%CZFe(x)/Al_2O_3 (x = 0, 0.1, 0.15, 0.2) catalysts.

Table 1.1. Measured compositions and BET surface areas of the 11.3wt%PdO/20wt%CZFe(x)/Al_2O_3 (x = 0, 0.1, 0.15, 0.2) catalysts

Catalyst	Measured composition	BET surface area ($m^2 \cdot g^{-1}$)
11.3wt%PdO/ 20wt%CZFe(0.2)/Al_2O_3	11.6wt%PdO/ 21wt%$Ce_{0.62}Zr_{0.18}Fe_{0.20}O_{2.0-\delta}$/γ-$Al_2O_3$	183
11.3wt%PdO/ 20wt%CZFe(0.15)/Al_2O_3	11.5wt%PdO/ 23wt%$Ce_{0.69}Zr_{0.16}Fe_{0.15}O_{2.0-\delta}$/γ-$Al_2O_3$	187
11.3wt%PdO/ 20wt%CZFe(0.1)/Al_2O_3	11.6wt%PdO/ 22wt%$Ce_{0.69}Zr_{0.20}Fe_{0.11}O_{2.0-\delta}$/γ-$Al_2O_3$	190
11.3wt%PdO/ 20wt%CZ/Al_2O_3	11.5wt%PdO/ 20wt%$Ce_{0.79}Zr_{0.21}O_{2.0-\delta}$/γ-$Al_2O_3$	219

Figure 1.2 shows the temperature dependences for methane conversion over the 11.3wt% PdO/20wt%CZFe(*x*)/Al_2O_3 (*x* = 0. 0.1, 0.15, 0.2) catalysts. By introducing Fe_2O_3, the catalytic activity was increased, and the highest catalytic activity was obtained for 11.3wt%PdO/20wt%CZFe(0.15)/Al_2O_3, which completely oxidized methane at a temperature as low as 310 °C. In contrast, 11.3wt%PdO/20wt%CZFe(0.2)/Al_2O_3 showed lower activity compared to 11.3wt%PdO/20wt%CZFe(0.15)/Al_2O_3 due to the low surface area.

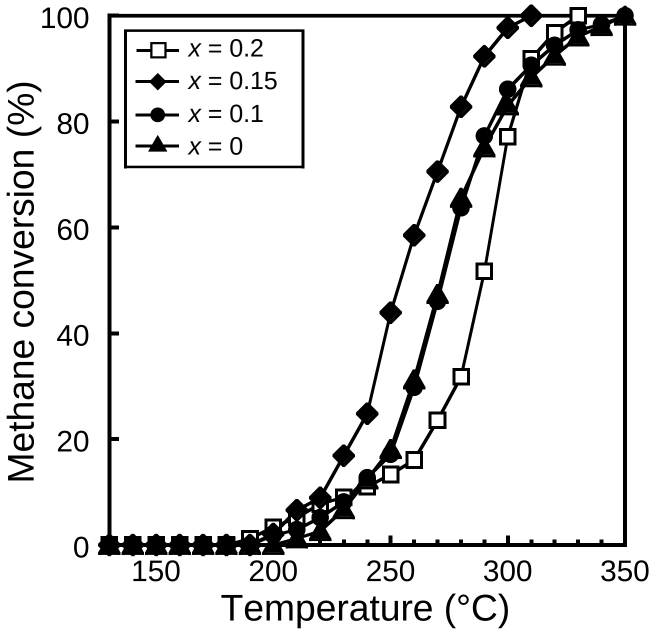

Figure 1.2. Temperature dependencies of methane oxidation over the 11.3wt%PdO/20wt%CZFe(*x*)/Al_2O_3 (*x* = 0. 0.1, 0.15, 0.2) catalysts.

Figure 1.3 shows the temperature dependences for methane conversion over the 11.3wt%PdO/(10–25)wt%CZFe(0.15)/γ-Al_2O_3 catalysts. The highest activity was obtained for the 11.3wt%PdO/16wt%CZFe(0.15)/γ-Al_2O_3 catalysts, and complete oxidation of methane was realized at 280 °C. Therefore, the optimum amount of CZFe(0.15) was determined to be 16wt%.

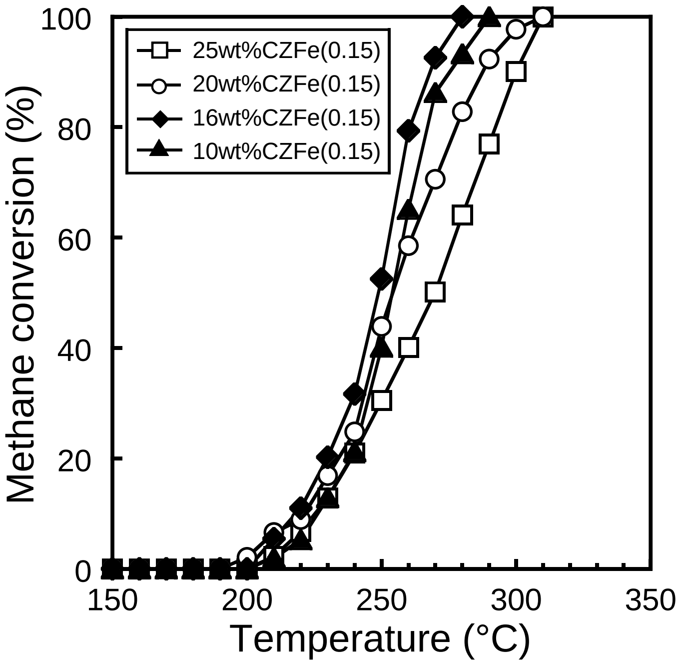

Figure 1.3. Temperature dependencies of methane oxidation over the 11.3wt%PdO/(10–25)wt%CZFe(0.15)/γ-Al_2O_3 catalysts.

Figure 1.4 shows the temperature dependences for methane conversion over the (8.0–13.6)wt%PdO/16wt%CZFe(0.15)/Al_2O_3 catalysts. Since the highest activity was obtained for the 11.3wt%PdO/16wt%CZFe(0.15)/Al_2O_3 catalysts, the optimum amount of PdO was 11.3wt%. When PdO was added more than 11.3wt%, catalytic activities decreased, likely due to the aggregation of PdO.

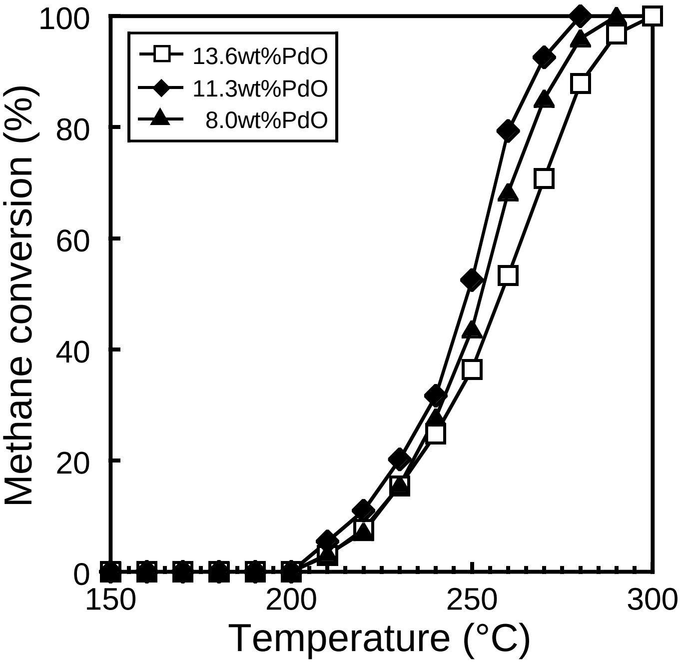

Figure 1.4. Temperature dependencies of methane oxidation over the (8.0–13.6)wt%PdO/16wt% CZFe(0.15)/Al_2O_3 catalysts.

Figure 1.5 shows the temperature dependences of methane conversion over the 11.3wt%PdO/16wt%CZFe(0.15)/Al_2O_3 (PdO/CZFe/Al_2O_3), 11.3wt%PdO/16wt%CZBi (0.15)/Al_2O_3 (PdO/CZBi/Al_2O_3), and 11.3wt%PdO/16wt%CZ/Al_2O_3 (PdO/CZ/Al_2O_3) catalysts. The catalytic methane oxidation activity was facilitated by introducing Bi_2O_3 or Fe_2O_3 into the CeO_2–ZrO_2 lattice as a promoter. In addition, the catalytic activity of PdO/CZFe/Al_2O_3 was significantly higher than that of PdO/CZBi/Al_2O_3. The reason for the high catalytic activity of PdO/CZFe/Al_2O_3 is that the oxygen release and storage abilities are improved due to the increase of oxygen vacancies and the redox property of $Fe^{3+/2+}$ ions. For the PdO/CZFe/Al_2O_3 catalyst, methane was completely oxidized at a temperature as low as 280 °C, which is 70 °C lower than that for PdO/CZ/Al_2O_3 (350 °C). Furthermore, the activity of PdO/CZFe/Al_2O_3 was also higher than that of the previous 11.6wt% PdO/15wt%$Ce_{0.62}Zr_{0.17}Bi_{0.21}O_{1.89}$/γ-$Al_2O_3$ catalyst (320 °C) [21].

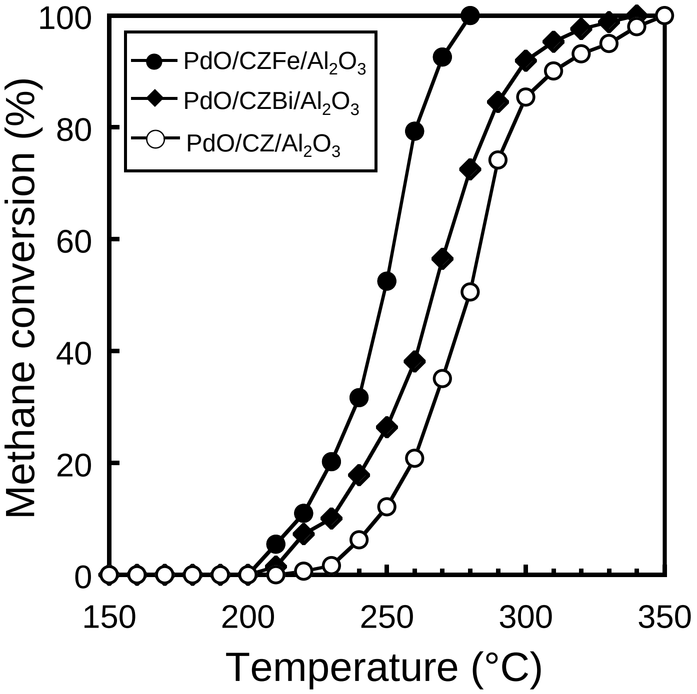

Figure 1.5. Temperature dependencies of methane oxidation over PdO/CZFe/Al_2O_3, PdO/CZBi/Al_2O_3, and PdO/CZ/Al_2O_3 catalysts.

As for the catalytic activity, methane conversions at each temperature were recorded under steady-state conditions. As an example, Figure 1.6 shows the methane conversion of PdO/CZFe/Al_2O_3 with time on stream at each temperature. After 20 min, the conversions were maintained, suggesting that the reactions are in steady-state.

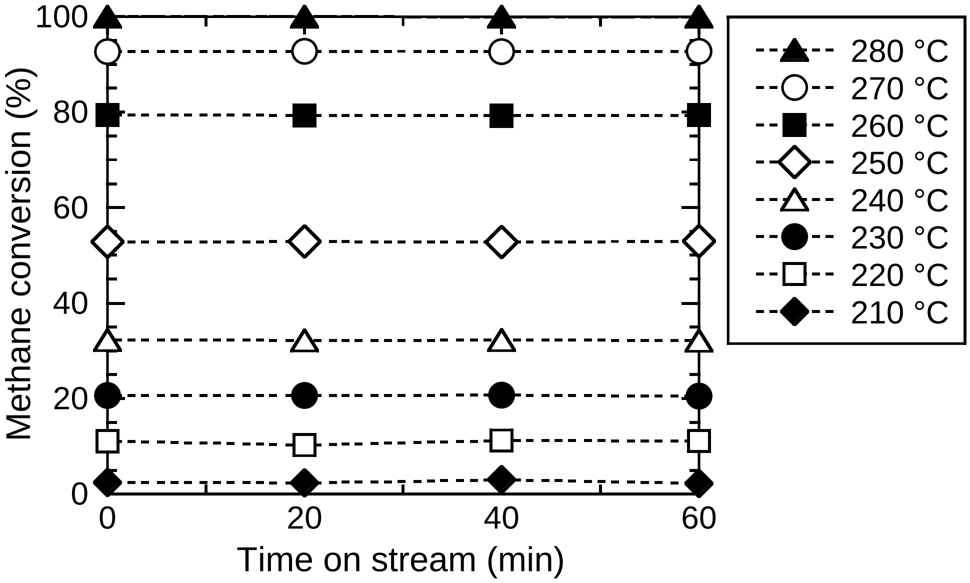

Figure 1.6. The methane conversion with time on stream over the PdO/CZFe/Al_2O_3 catalyst.

TPR measurements were conducted to investigate the oxygen release abilities. Figure 1.7 shows the TPR results for PdO/CZFe/Al_2O_3, PdO/CZBi/Al_2O_3, and PdO/CZ/Al_2O_3 catalysts. The reduction peak temperatures are summarized in Table 1.3. The reduction temperature of PdO/CZBi/Al_2O_3 (−2 °C) was lower than that for PdO/CZ/Al_2O_3 (9 °C) due to the generation of oxygen vacancies for oxide ion mobility. The reduction temperature of PdO/CZFe/Al_2O_3 (−13 °C) was lower than those of PdO/CZBi/Al_2O_3 and PdO/CZ/Al_2O_3. This easier reduction for the PdO/CZFe/Al_2O_3 catalyst is related to the increase of oxide ion mobility and the enhancement of the redox property. It is considered that the redox property for PdO/CZFe/Al_2O_3 is effectively improved by the valence changes of $Fe^{3+/2+}$, compared with the case for the introduction of Bi^{3+} into PdO/CZBi/Al_2O_3. Therefore, Fe_2O_3 doping into the CeO_2–ZrO_2 lattice is effective for improving the oxygen supply capability at low temperatures. In addition, the OSC results of the PdO/CZFe/Al_2O_3, PdO/CZBi/Al_2O_3, and PdO/CZ/Al_2O_3 catalysts are also tabulated in Table 1.5. The OSC of PdO/CZFe/Al_2O_3 was significantly larger than those of PdO/CZBi/Al_2O_3 and PdO/CZ/Al_2O_3. Consequently, it is clear that the PdO/CZFe/Al_2O_3 catalyst possessed high oxygen release and storage abilities.

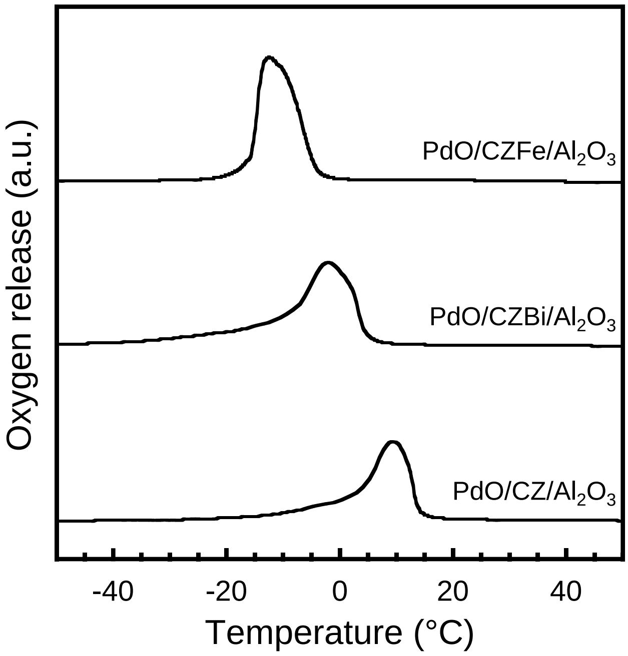

Figure 1.7. TPR profiles of PdO/CZFe/Al_2O_3, PdO/CZBi/Al_2O_3, and PdO/CZ/Al_2O_3.

Table 1.2. Reduction temperature and OSC of PdO/CZFe/Al_2O_3, PdO/CZBi/Al_2O_3 and PdO/CZ/Al_2O_3

Catalyst	Reduction temperature (°C)	OSC (μmol·O_2 g^{-1})
PdO/CZFe/Al_2O_3	−13	241
PdO/CZBi/Al_2O_3	−2	144
PdO/CZ/Al_2O_3	9	115

1.3.2 PdO/CeO_2–ZrO_2–NiO/γ-Al_2O_3 catalyst

Figure 1.8 shows the XRD patterns of the 11.3wt%PdO/20wt%$Ce_{0.8(1-x)}Zr_{0.2(1-x)}Ni_xO_{2.0-\delta}$/γ-$Al_2O_3$ (11.3wt%PdO/20wt%CZNi(x)/Al_2O_3) (x = 0, 0.1, 0.2) catalysts. The phase of PdO, cubic fluorite-type, and a γ-Al_2O_3 phase were observed, and crystalline impurities were not confirmed.

The measured compositions and BET specific surface areas of the 11.3wt%PdO/20wt%CZNi(x)/Al_2O_3 (x = 0, 0.1, 0.2) catalysts are tabulated in Table 1.3. The measured compositions are in good agreement with the stoichiometric values within the experimental error. The BET specific surface areas of 11.3wt%PdO/20wt%CZNi(x)/Al_2O_3 were lower than that of 11.3wt%PdO/16wt%CZ/Al_2O_3, likely due to the lower melting point of NiO (1998 °C) [24] compared to CeO_2 (2445 °C) [23] and ZrO_2 (2710 °C) [23].

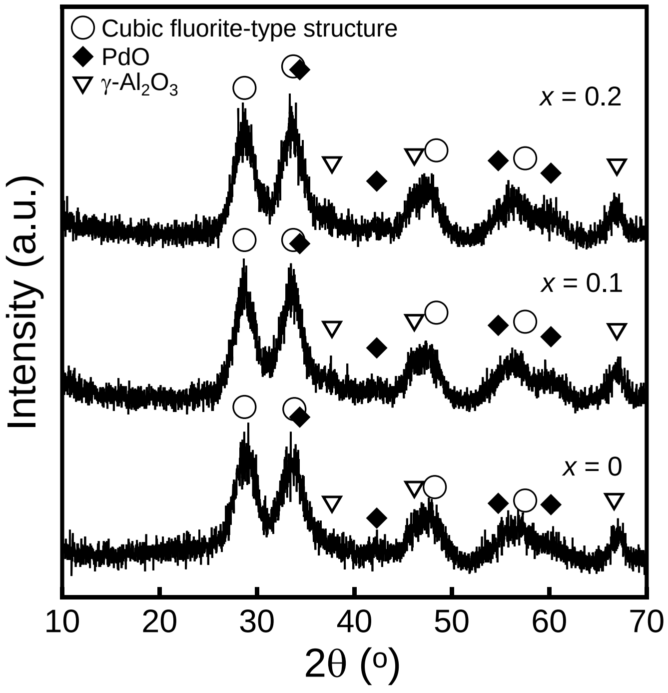

Figure 1.8. XRD patterns of the 11.3wt%PdO/20wt%CZNi(x)/Al_2O_3 (x = 0, 0.1, 0.2) catalysts.

Table 1.3. Measured compositions and BET surface areas of the 11.3wt%PdO/20wt%CZNi(*x*)/Al_2O_3 ($x = 0, 0.1, 0.2$) catalysts

Catalyst	Measured composition	BET surface area ($m^2 \cdot g^{-1}$)
11.3wt%PdO/ 16wt%CZNi(0.2)/Al_2O_3	10.7wt%PdO / 19wt%$Ce_{0.66}Zr_{0.16}Ni_{0.18}O_{2.0-\delta}$/γ-$Al_2O_3$	175
11.3wt%PdO/ 16wt%CZNi(0.1)/Al_2O_3	11.6wt%PdO / 20wt%$Ce_{0.72}Zr_{0.19}Ni_{0.09}O_{2.0-\delta}$/γ-$Al_2O_3$	185
11.3wt%PdO/ 16wt%CZ/Al_2O_3	11.5wt%PdO / 20wt%$Ce_{0.79}Zr_{0.21}O_{2.0-\delta}$/γ-$Al_2O_3$	219

Figure 1.9 shows the temperature dependences for methane conversion over the 11.3wt% PdO/20wt%CZNi(*x*)/Al_2O_3 (x = 0. 0.1, 0.2) catalysts. By introducing NiO, the catalytic activity was increased, and the highest catalytic activity was obtained for 11.3wt%PdO/20wt%CZNi(0.2)/Al_2O_3, which completely oxidized methane at a temperature as low as 300 °C.

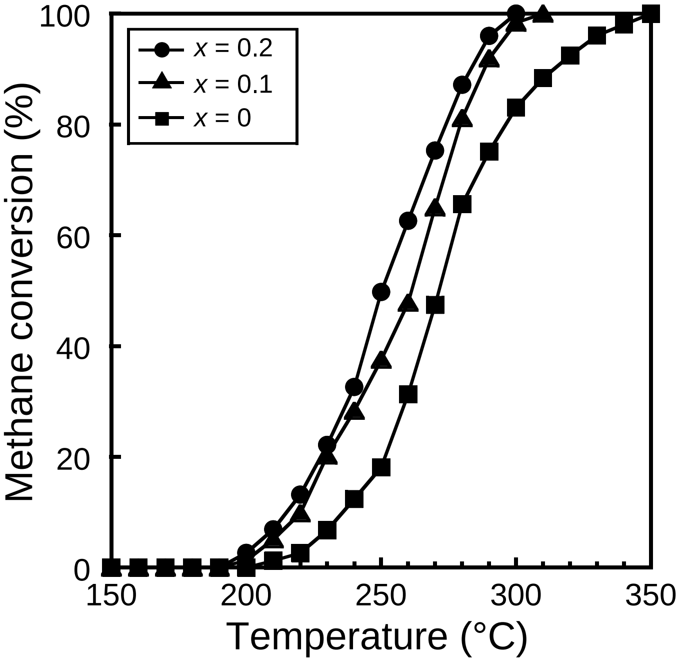

Figure 1.9. Temperature dependencies of methane oxidation over the 11.3wt%PdO/20wt% CZNi(*x*)/Al_2O_3 (x = 0. 0.1, 0.2) catalysts.

Figure 1.10 shows the temperature dependences for methane conversion over the 11.3wt%PdO/(16–25)wt%CZNi(0.2)/Al_2O_3 catalysts. Since, the highest activity was obtained for the 11.3wt%PdO/20wt%CZNi(0.2)/Al_2O_3 catalysts, the optimum amount of CZNi(0.2) was determined to be 20wt%.

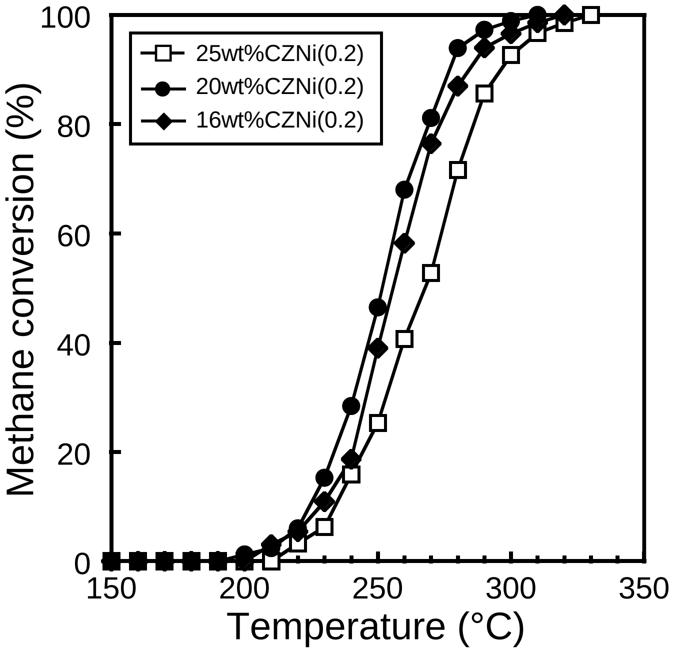

Figure 1.10. Temperature dependencies of methane oxidation over the 11.3wt%PdO/(16–25)wt% CZNi(0.2)/Al_2O_3 catalysts.

Figure 1.11 shows the temperature dependences for methane conversion over the (8.0–13.6)wt%PdO/20wt%CZNi(0.2)/Al_2O_3 catalysts. Since the highest activity was obtained for the 11.3wt%PdO/20wt%CZNi(0.2)/Al_2O_3 catalysts, the optimum amount of PdO was 11.3wt%. When PdO was added more than 11.3wt%, catalytic activities decreased, likely due to the aggregation of PdO.

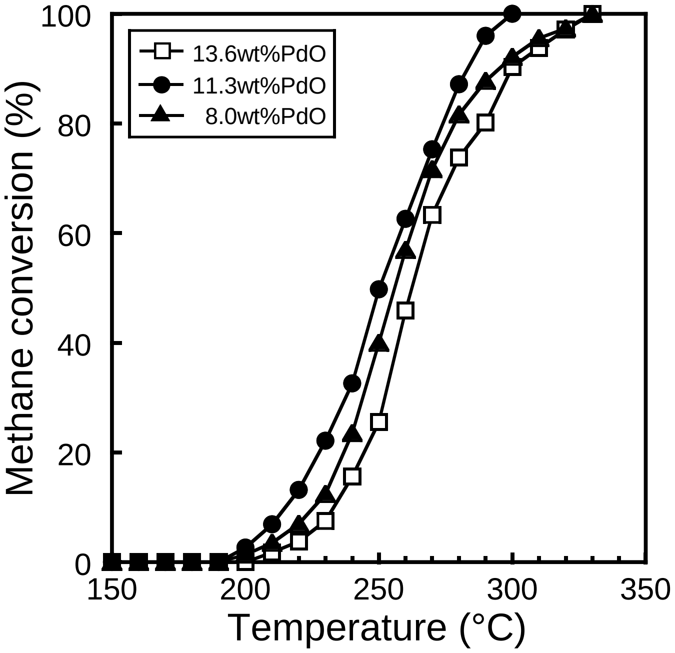

Figure 1.11. Temperature dependencies of methane oxidation over the (8.0–13.6)wt%PdO/20wt%CZNi(0.2)/Al_2O_3 catalysts.

Figure 1.12 shows the temperature dependences for methane conversion over the 11.3wt%PdO/20wt%CZNi(0.2)/Al_2O_3 (PdO/CZNi/Al_2O_3), PdO/CZFe/Al_2O_3, and PdO/CZ/Al_2O_3 catalysts. The PdO/CZNi/Al_2O_3 catalyst exhibited high catalytic activity compared to PdO/CZ/Al_2O_3 by introducing NiO into the CeO_2–ZrO_2 lattice, and methane was completely oxidized at 300 °C, which was lower than those of PdO/CZ/Al_2O_3 (350 °C) and previous 11.6wt%PdO/15wt%$Ce_{0.62}Zr_{0.17}Bi_{0.21}O_{1.89}$/γ-$Al_2O_3$ catalyst (320 °C) [21]. However, the activity of PdO/CZNi/Al_2O_3 was lower than that of PdO/CZFe/Al_2O_3.

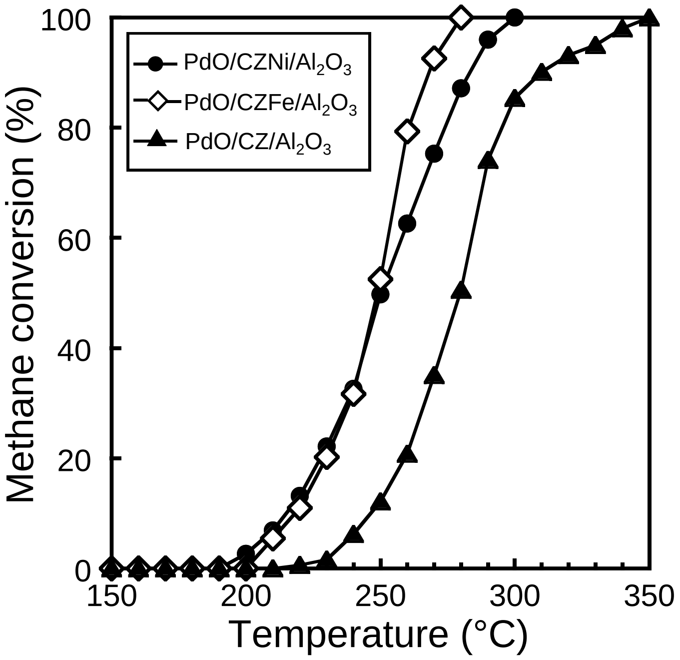

Figure 1.12. Temperature dependencies of methane oxidation over the PdO/CZNi/Al_2O_3, PdO/CZFe/Al_2O_3, and PdO/CZ/Al_2O_3 catalysts.

In order to investigate the oxygen release and storage abilities of PdO/CZNi/Al_2O_3, TPR measurements were carried out (Figure 1.13). The reduction peak temperature is summarized in Table 1.4 with the data of PdO/CZFe/Al_2O_3, PdO/CZBi/Al_2O_3, and PdO/CZ/Al_2O_3. The reduction temperature of PdO/CZNi/Al_2O_3 (−11 °C) was lower than those of PdO/CZBi/Al_2O_3 and PdO/CZ/Al_2O_3. This easier reduction for the PdO/CZNi/Al_2O_3 catalyst is related to the increase of oxide ion mobility and the enhancement of the redox property. It is considered that the redox property for PdO/CZNi/Al_2O_3 is effectively improved by the valence changes of $Ni^{3+/2+}$, compared with the case for the introduction of Bi^{3+} into PdO/CZBi/Al_2O_3. Accordingly, NiO doping into the CeO_2–ZrO_2 lattice is effective for improving the oxygen supply capability at low temperatures. In addition, the OSC results of the PdO/CZNi/Al_2O_3, PdO/CZFe/Al_2O_3, PdO/CZBi/Al_2O_3, and PdO/CZ/Al_2O_3 catalysts are also tabulated in Table 1.4. The OSC of PdO/CZNi/Al_2O_3 was significantly larger than those of PdO/CZBi/Al_2O_3 and PdO/CZ/Al_2O_3. Therefore, it is clear that the PdO/CZNi/Al_2O_3 catalyst exhibited high oxygen release and storage abilities. For comparison with the results for PdO/CZFe/Al_2O_3, PdO/CZNi/Al_2O_3 showed the higher reduction temperature and the lower OSC value, supporting that the catalytic activity of PdO/CZNi/Al_2O_3 was lower than that of PdO/CZFe/Al_2O_3.

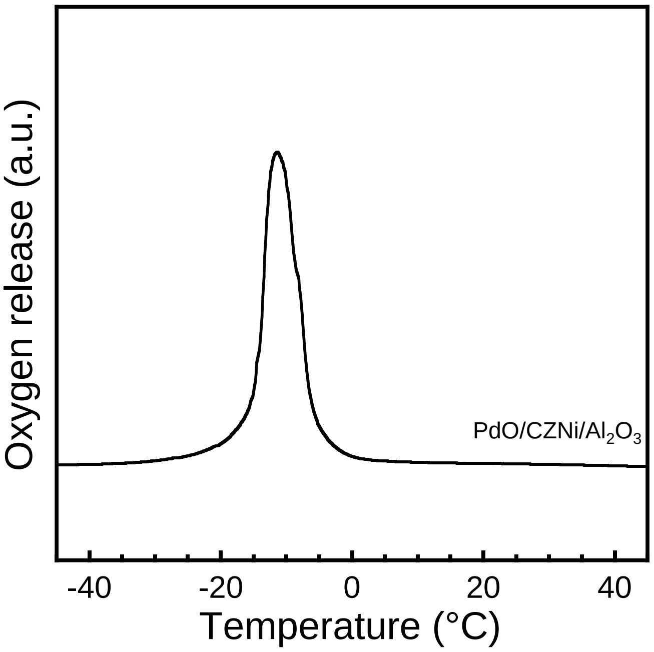

Figure 1.13. TPR profile of PdO/CZNi/Al_2O_3.

Table 1.4. Reduction temperature and OSC of PdO/CZNi/Al_2O_3, PdO/CZFe/Al_2O_3, PdO/CZBi/Al_2O_3, and PdO/CZ/Al_2O_3

Catalyst	Reduction temperature (°C)	OSC (μmol·O_2 g^{-1})
PdO/CZNi/Al_2O_3	−11	220
PdO/CZFe/Al_2O_3	−13	241
PdO/CZBi/Al_2O_3	−2	144
PdO/CZ/Al_2O_3	9	115

1.4 Conclusions

In this chapter, for methane complete oxidation at moderate temperatures, Fe_2O_3 and NiO were introduced into the CeO_2–ZrO_2 lattice to increase the oxygen release and storage abilities. The introduction of Fe_2O_3 and NiO into the CeO_2–ZrO_2 lattice as a promoter was found to effectively enhance the oxygen release and storage abilities due to the formation of oxygen vacancies and the redox of $Fe^{3+/2+}$ or $Ni^{3+/2+}$ ions. These CeO_2–ZrO_2–MO_x (M = Fe, Ni) promoters facilitated the catalytic oxidation on PdO activator. Among the samples prepared, the 11.3wt%PdO/16wt%$Ce_{0.68}Zr_{0.17}Fe_{0.15}O_{2.0-\delta}$/γ-$Al_2O_3$ and 11.3wt%PdO/20wt%$Ce_{0.64}Zr_{0.16}Ni_{0.2}O_{2.0-\delta}$/γ-$Al_2O_3$ catalysts were found to achieve the complete methane oxidation at the temperatures as low as 280 °C and 300 °C, respectively, which were lower than that of the previous 11.6wt%PdO/15wt%$Ce_{0.62}Zr_{0.17}Bi_{0.21}O_{1.89}$/γ-$Al_2O_3$ catalyst (320 °C).

Chapter 2

Effect of Conductivities in CeO_2–ZrO_2 Based Promoters on Catalytic Activities

2.1 Introduction

In the previous chapter, it was demonstrated that the catalytic methane oxidation was successfully facilitated by CeO_2–ZrO_2–MO_x (M = Fe, Ni) promoters, and methane was completely oxidized at 280 °C (PdO/CeO_2–ZrO_2–Fe_2O_3/Al_2O_3) and 300 °C (PdO/CeO_2–ZrO_2–NiO/Al_2O_3). The enhancements might be related to the oxide ion conductivity and the redox property of the promoter; however, the relationships between these properties, oxygen release and storage abilities, and the catalytic activity still remain unclear.

In this chapter, these relationships by comparing the ionic conductivities and redox properties of various ceria–zirconia based promoters, CeO_2–ZrO_2–MO_x (M = Bi, Ca, Sn, Ni, Fe), were investigated using electrochemical techniques. The oxygen release and storage abilities were characterized using CeO_2–ZrO_2–MO_x supported on γ-Al_2O_3. The catalytic activities for methane oxidation were investigated for PdO/CeO_2–ZrO_2–MO_x/Al_2O_3 (M = Bi, Ca, Sn, Ni, Fe) catalysts.

2.2 Experimental Procedure

16wt%$Ce_{0.68}Zr_{0.17}M_{0.15}O_{2.0-\delta}/\gamma-Al_2O_3$ (CZM/Al_2O_3) (M = Bi, Ca, Sn, Ni, Fe) samples were synthesized by the conventional wet coprecipitation method. Prior to preparation, commercial $\gamma-Al_2O_3$ (AxSorb AB, Nippon Light Metal) was ground in an agate mortar and then mechanically pulverized by a ball-milling apparatus (Pulverisette 7, FRITSCH GmbH) at the rotation speed of 300 rpm for 3 h. Stoichiometric mixture of 1.0 $mol\cdot L^{-1}$ $Ce(NO_3)_3$, 0.1 $mol\cdot L^{-1}$ $ZrO(NO_3)_2$, and 0.1 $mol\cdot L^{-1}$ $Bi(NO_3)_3$ (or $Ca(NO_3)_2$, $Fe(NO_3)_3$, $Ni(NO_3)_2$) or SnC_2O_4 was dissolved into the 15 mL of 3 $mol\cdot L^{-1}$ nitric acid, and $\gamma-Al_2O_3$ powder was added. The mixture was stirred at room temperature for 30 min and its pH was adjusted to 11 by the dropwise addition of 6% ammonia in aqueous solution. After stirring for 12 h at room temperature, the resulting precipitate was collected by filtration, washed several times with deionized water, and then dried at 80 °C for 6 h. Subsequently, these powders were calcined at 500 °C for 1 h under air. 16 wt%$Ce_{0.8}Zr_{0.2}O_{2.0-\delta}/\gamma-Al_2O_3$ (CZ/Al_2O_3) was also prepared by the same coprecipitation method. Catalysts composed of palladium supported on the CZM/Al_2O_3 were prepared by the impregnation of the CZM/Al_2O_3 samples with a $Pd(NO_2)_2(NH_3)_2$ solution (Tanaka Kikinzoku Kogyo) followed by drying at 80 °C for 12 h and then calcination at 400 °C for 4 h to obtain 11.3wt%PdO/16wt%$Ce_{0.68}Zr_{0.17}M_{0.15}O_{2.0-\delta}/\gamma-Al_2O_3$ ($PdO/CZM/Al_2O_3$). For the Rietveld analyses and electrochemical measurements, $Ce_{0.68}Zr_{0.17}M_{0.15}O_{2.0-\delta}$ (CZM) (M = Bi, Ca, Sn, Ni, Fe) and CZ solids were prepared by the coprecipitation method identical with the above method without using the $\gamma-Al_2O_3$ support, and the powders were calcined at 700 °C for 1 h.

X-ray photoelectron spectroscopy (XPS; PHI5000 VersaProbe II, ULVAC-PHI) was performed at room temperature using Al Kα radiation (1486.6 eV) without Ar ion etching. Pellet samples of 5 mm diameter were prepared from powders and placed into an ultrahigh vacuum chamber at 10^{-7} Pa for the XPS analysis. The effect of charging on the binding energies was corrected with respect to the C 1s peak at 284.6 eV, and spectra were fitted using a Shirley background and a

Gaussian–Lorentzian function. X-ray powder diffraction (XRD; SmartLab, Rigaku) patterns were measured using Cu Kα radiation (40 kV, 30 mA) over the 2θ range from 10 to 70° with a step size of 0.02° and a scan speed of $2°\cdot\mathrm{min}^{-1}$. The crystallite size of PdO was determined by the Scherrer equation. For Rietveld analysis, XRD data (MultiFlex, Rigaku) were also recorded over the 2θ range from 10 to 150° with a step size of 0.02° for a count time of 5 sec using Cu Kα radiation (40 kV, 40 mA). Structural parameters, such as the lattice parameter and oxygen occupancy, were determined by Rietveld refinements using the RIETAN-FP software package [25].

For the conductivity and the open circuit electoromotive force (EMF) measurement, CZM (M = Bi, Ca, Sn, Ni, Fe) and CZ were made into pellets using uniaxial pressing, and then, the pellets were sintered at 700 °C for 5 h in the air flow. After the sintering process, the AC conductivity (σ_{AC}) values of the pellets were determined via a complex impedance technique (1260 impedance/gain analyzer, Solartron) over the temperature range from 700 to 300 °C. The ionic transference number (t_{i}) of each specimen was determined using an oxygen concentration cell with the construction: O_2, Pt │ sample │Pt, air. EMF data were acquired with an electrometer (R8240, Advantest) at temperatures between 700 and 500 °C. If the sample is a pure oxide-ionic conductor, theoretical EMF ($E_{\mathrm{theoretical}}$) is calculated by following equation:

$$E_{\mathrm{theoretical}} = \frac{RT}{4F}\ \ln\left(\frac{P\mathrm{o}_2}{P_{\mathrm{Air}}}\right) ,$$

where R, T, F, $P\mathrm{o}_2$ and P_{Air} are the gas constant, absolute temperature, Faraday constant, oxygen partial pressure, and air partial pressure, respectively. This $E_{\mathrm{theoretical}}$ together with the experimentally measured EMF (E_{mea}) can be used to calcuate t_{i} ($t_{\mathrm{i}} = E_{\mathrm{mea}} / \mathrm{E}_{\mathrm{theoretical}}$). t_{i} can also be determined using the equation:

$$t_{\mathrm{i}} = \frac{\sigma_{\mathrm{ion}}}{\sigma_{\mathrm{ion}} + \sigma_{\mathrm{e}^-}} = \frac{\sigma_{\mathrm{ion}}}{\sigma_{\mathrm{AC}}} ,$$

where σ_{ion} is the ionic conductivity of the sample and $\sigma_{\mathrm{e^-}}$ is the electronic conductivity. If the conducting species are oxide ions and/or electrons, the oxide-ionic conductivity ($\sigma_{\mathrm{O^{2-}}}$) and $\sigma_{\mathrm{e^-}}$ can be estimated using the following equations

$$\sigma_{\mathrm{O^{2-}}} = t_{\mathrm{i}} \cdot \sigma_{\mathrm{AC}}$$

$$\sigma_{\mathrm{e^-}} = (1 - t_{\mathrm{i}}) \cdot \sigma_{\mathrm{AC}}$$

Temperature-programmed reduction (TPR) measurement was carried out under a flow of 5 vol% hydrogen–argon (50 mL·min^{-1}) at a heating rate of 5 °C·min^{-1} up to 510 °C (BELCAT-B, MicroTracBEL) and then, the oxygen storage capacity (OSC) was carried out using the pulse-injection method at 427 °C. X-ray fluorescence (XRF; ZSX100e, Rigaku) was used to determine the compositions of the catalysts. Brunauer–Emmett–Teller (BET) specific surface areas were acquired by nitrogen adsorption at −196 °C (TriStar 3000, Shimadzu). The PdO dispersion analysis was carried out using a pulse method at −50 °C with 10% carbon monoxide-helium (0.03 mL) by the same apparatus (BELCAT, MicroTracBEL).

The methane oxidation activity was tested in a conventional fixed-bed flow reactor consisting of a quartz glass tube (diameter = 10 mm) with a feed gas mixture of 1 vol% methane–air at a rate of 33.4 mL·min^{-1} over 0.1 g of catalyst. Here, the space velocity was calculated to be 20,000 L·kg^{-1}·h^{-1}. The catalysts were pretreated at 200 °C for 2 h under argon flow (20 mL·min^{-1}) before the catalytic activity tests. The catalytic activity was evaluated in terms of the approximately-constant methane conversion at each temperature maintained for over an hour. The gas composition after the reaction was analyzed using gas chromatography with Molecular Sieve 5A column and thermal conductivity detection (GC-8AIT, Shimadzu).

2.3 Results and Discussion

Figure 2.1 shows the results of the Rietveld refinements of XRD patterns for the CZM (M = Bi, Ca, Sn, Ni, Fe) and CZ promoters. The XRD patterns of CZM and CZ displayed diffraction peaks of a fluorite-type structure with the space group $Fm\overline{3}m$, while a small amount of an additional fluorite-type phase was observed in the CZM (M = Bi, Ca, Sn, Ni, Fe) promoters, caused by the decomposition of the main phase due to the high-temperature calcination to increase the crystallinity. The structure parameters of main cubic fluorite-type phase for CZM and CZ are presented in Table 2.1. The occupancies of each cation were comparable with the expected stoichiometric values. The lattice parameters of the CZM (M = Bi, Ca) samples were larger than that of CZ, because larger Bi^{3+} (0.117 nm) [26] or Ca^{2+} (0.126 nm) [26] ions partially occupied Ce^{4+} (0.097 nm) [26] and Zr^{4+} (0.084 nm) [26] sites. Conversely, since the ionic radii of Sn^{4+} (0.095 nm) [26], Ni^{2+} (0.072 nm) [27] and Fe^{3+} (0.078 nm) [26] are smaller than those of Ce^{4+} and Zr^{4+}, lattice shrinkage was confirmed for the CZM (M = Sn, Ni, Fe) samples.

As listed in Table 2.1, the oxygen occupancies of the CZM (M = Bi, Ca, Sn, Ni, Fe) and CZ solids were all below 1, indicating the generation of oxygen vacancies. The oxygen occupancy in CZBi was lower than that in CZ because the partial substitution of the lower valency Bi^{3+} ions at the tetravalent Ce^{4+} and Zr^{4+} sites formed additional oxygen vacancies via the charge compensation mechanism. The oxygen occupancy of CZCa was decreased compared to that of CZBi, demonstrating that additional oxygen vacancies were formed due to the introduction of divalent Ca^{2+} ions instead of trivalent Bi^{3+} ions. From the occupancies of the constituent ions, the Ce^{4+}:Ce^{3+} ratios in CZBi and CZCa were calculated to be 75:25 and 77:23, both of which are similar to that for CZ (Ce^{4+}:Ce^{3+} = 79:21). In addition, increase of oxygen vacancies in CZSn compared to that in CZ was observed. Since the Sn ions were tetravalent (Figure 2.2), the Ce^{4+}:Ce^{3+} ratio was estimated to be 61:39. The oxygen occupancy results for CZNi and CZFe revealed the formation of additional oxygen vacancies compared to the CZBi case, because the dopant cations in CZNi and CZFe partially were reduced to divalent state from trivalent state. Assuming that CZBi and CZM (M = Ni and Fe) had the same Ce^{4+}:Ce^{3+} ratio, the Ni^{3+}:Ni^{2+} and Fe^{3+}:Fe^{2+} were approximately 18:82 and 5:95, respectively.

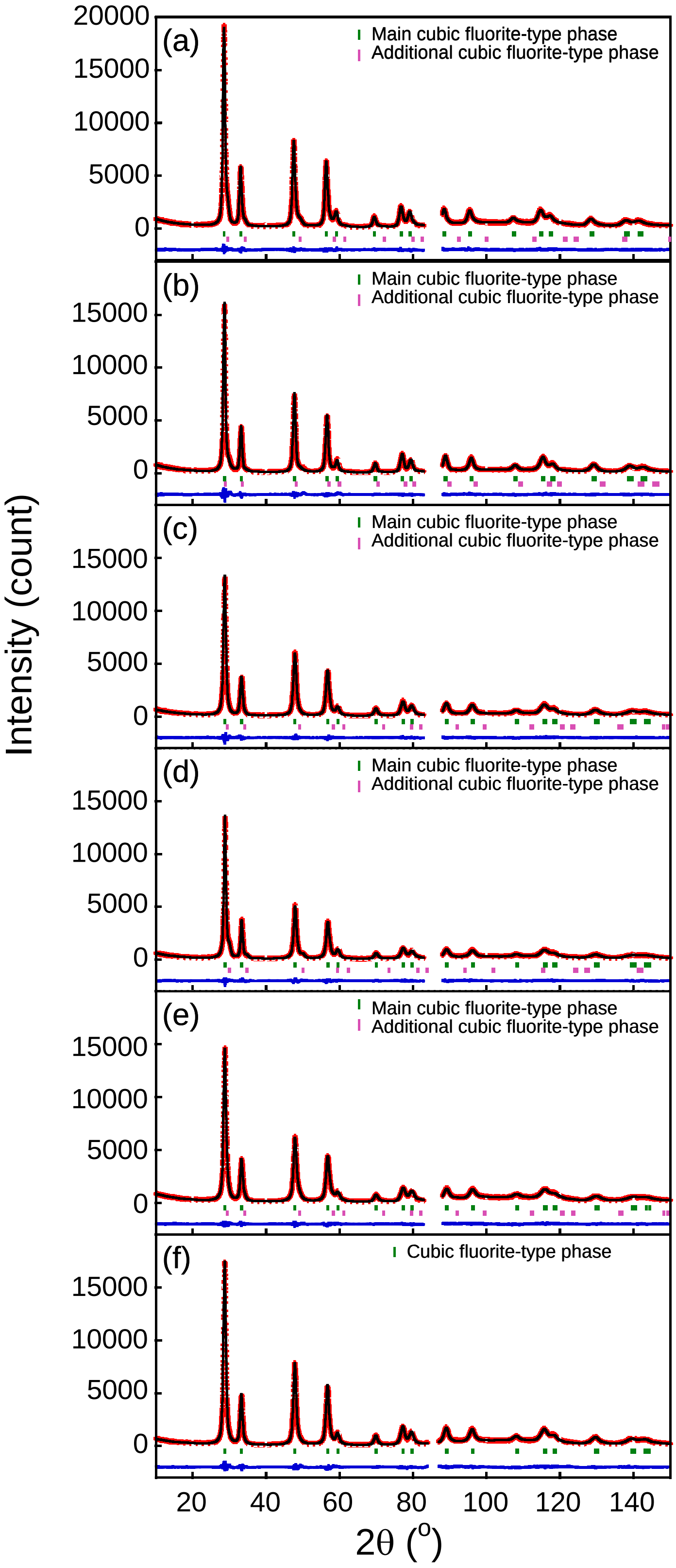

Figure 2.1. Results of Rietveld analyses of (a) CZBi, (b) CZCa, (c) CZSn, (d) CZNi, (e) CZFe, and (f) CZ.

Table 2.1. Structural parameters of the CZM (M = Bi, Ca, Sn, Ni, Fe) and CZ solids

Sample	Lattice parameter (nm)	Atom	Wyckoff position	*g*	*x*	*y*	*z*	*B* (Å^2)
CZBi	0.541095(5)	Ce	4*a*	0.680(1)	0	0	0	0.50
		Zr	4*a*	0.170(1)				
		Bi	4*a*	0.150(1)				
		O	8*c*	0.921(3)	1/4	1/4	1/4	0.58
Space group: $Fm\bar{3}m$, R_{wp} = 4.83%, S = 1.38								
CZCa	0.540030(5)	Ce	4*a*	0.681(1)	0	0	0	0.50
		Zr	4*a*	0.170(1)				
		Ca	4*a*	0.149(1)				
		O	8*c*	0.886(3)	1/4	1/4	1/4	0.89
Space group: $Fm\bar{3}m$, R_{wp} = 6.18%, S = 1.53								
CZSn	0.537977(5)	Ce	4*a*	0.681(1)	0	0	0	0.45
		Zr	4*a*	0.170(1)				
		Sn	4*a*	0.149(1)				
		O	8*c*	0.933(3)	1/4	1/4	1/4	0.44
Space group: $Fm\bar{3}m$, R_{wp} = 5.30%, S = 1.24								
CZNi	0.537871(6)	Ce	4*a*	0.690(1)	0	0	0	0.47
		Zr	4*a*	0.173(1)				
		Ni	4*a*	0.137(1)				
		O	8*c*	0.893(3)	1/4	1/4	1/4	0.85
Space group: $Fm\bar{3}m$, R_{wp} = 5.74%, S = 1.29								
CZFe	0.537865(6)	Ce	4*a*	0.677(1)	0	0	0	0.44
		Zr	4*a*	0.169(1)				
		Fe	4*a*	0.154(1)				
		O	8*c*	0.884(3)	1/4	1/4	1/4	0.84
Space group: $Fm\bar{3}m$, R_{wp} = 5.14%, S = 1.34								
CZ	0.538158(6)	Ce	4*a*	0.801(1)	0	0	0	0.50
		Zr	4*a*	0.200(1)				
		O	8*c*	0.958(3)	1/4	1/4	1/4	0.65
Space group: $Fm\bar{3}m$, R_{wp} = 5.74%, S = 1.55								

Constraints on occupation factors: g(Ce) / g(Zr) = 4 and g(Ce) + g(Zr) + g(M) = 1 (M = Bi, Ca, Sn, Ni, Fe)

Figure 2.2 shows the valence states of dopant cations in the CZM (M = Bi, Ca, Sn, Ni, Fe) solids which were investigated by XPS. The CZBi and CZCa solids generated peaks attributed to Bi^{3+} and Ca^{2+}, respectively. The Ni and Fe peaks generated by CZNi and CZFe can be attributed to both divalent and trivalent states, and the Ni^{3+}:Ni^{2+} and Fe^{3+}:Fe^{2+} ratios were determined to be 27:73 and 56:44, respectively, while the Sn ions in CZSn were found to have a single valence state equivalent to tetravalent Sn^{4+}.

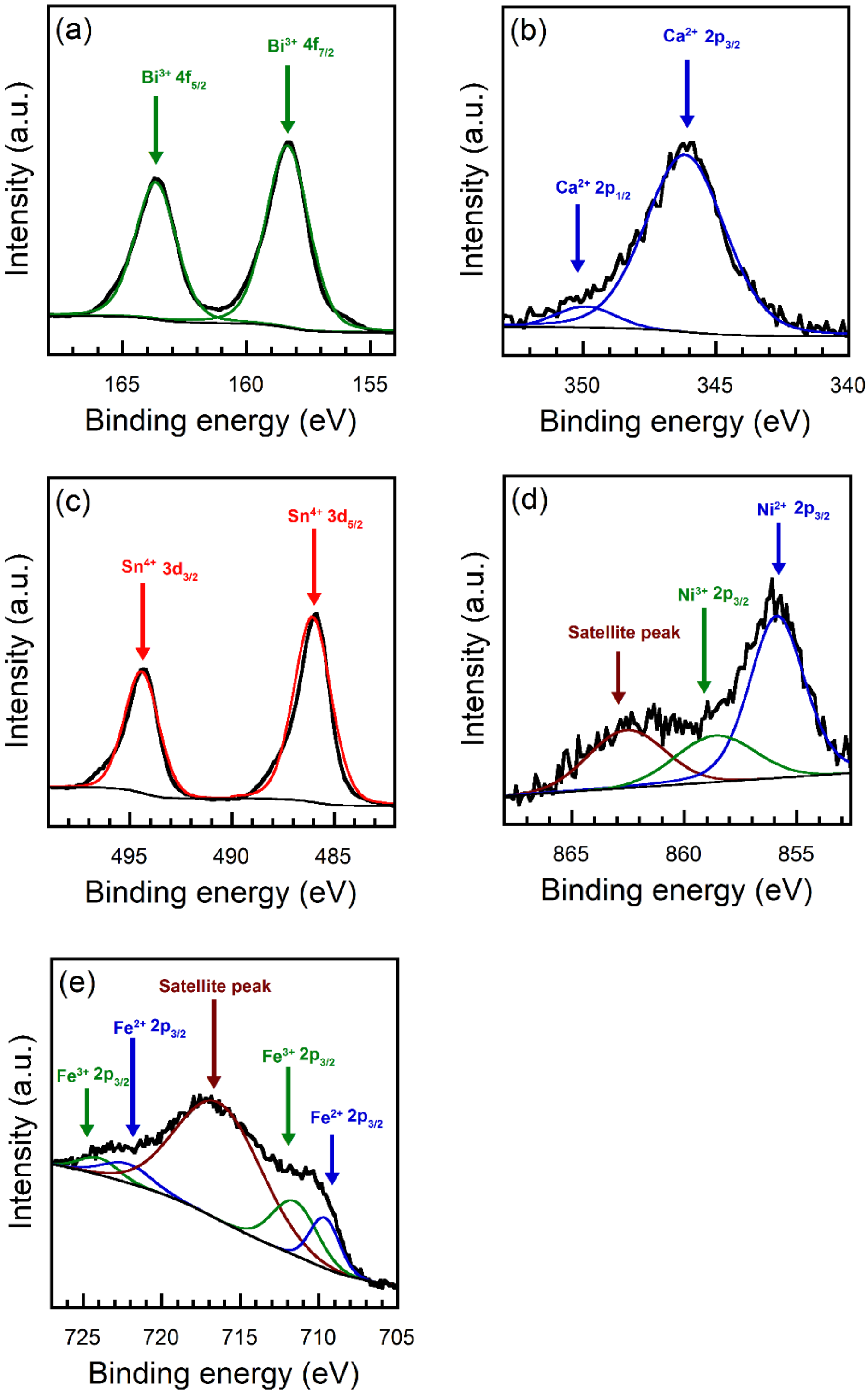

Figure 2.2. XPS spectra of (a) Bi 4f core-levels of CZBi, (b) Ca 2p core-levels of CZCa, (c) Sn 3d core-levels of CZSn, (d) Ni 2p core-levels of CZNi, and (e) Fe 2p core-levels of CZFe.

The AC conductivities of the CZM (M = Bi, Ca, Sn, Ni, Fe) and CZ solids as functions of temperature between 700 and 300 °C are shown in Figure 2.3. At each measuring temperature, the AC conductivities of CZM are higher than those of CZ. Because the AC conductivity is composed of both ionic and electronic conductivities, EMF measurements were measured using an oxygen gas concentration cell and the ionic transference numbers for these materials were calculated. Figure 2.4 shows the ionic transference numbers of the CZM and CZ samples over temperature range of 700 to 500 °C, since it is difficult to evaluate EMF values below 500 °C due to the high internal resistance. The ionic transference numbers of CZCa and CZBi are evidently increased compared to that of CZ because of the generation of oxygen vacancies which promote the migration of oxide ions. Conversely, the introduction of $Sn^{4+/2+}$, $Ni^{3+/2+}$, or $Fe^{3+/2+}$ ions into the CZ lattice decreased the ionic transference number, suggesting that the electronic conductivity was increased due to the valence changes of the $Sn^{4+/2+}$, $Ni^{3+/2+}$ and $Fe^{3+/2+}$ ions.

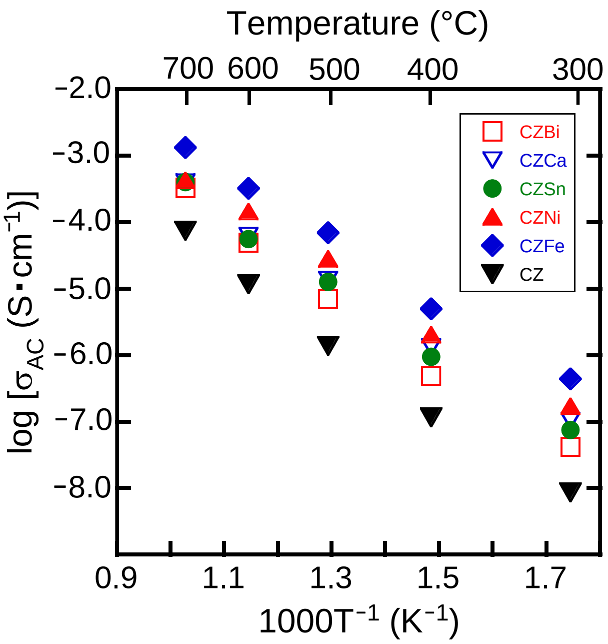

Figure 2.3. Temperature dependences of the AC conductivity values of the CZM (M = Bi, Ca, Sn, Ni, Fe) and CZ promoters.

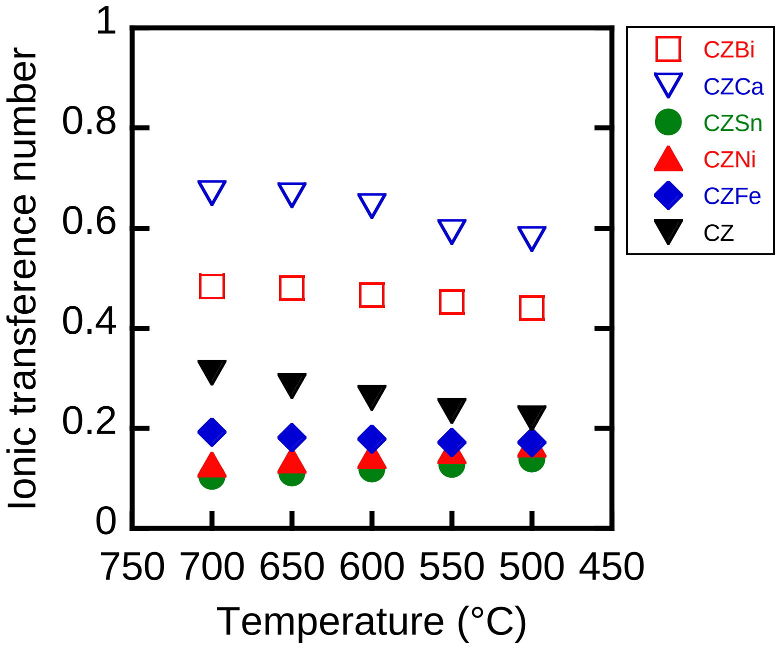

Figure 2.4. Temperature dependences of the ionic transference numbers of the CZM (M = Bi, Ca, Sn, Ni, Fe) and CZ solids.

Figure 2.5 shows the TPR profiles of the CZM/Al_2O_3 (M = Bi, Ca, Sn, Ni, Fe) and CZ/Al_2O_3 samples, and the reduction temperatures are provided in Table 2.2. In addition, OSC values were obtained from the CZM/Al_2O_3 and CZ/Al_2O_3 samples after the TPR analyses, and the results are also summarized in Table 2.2. By introducing lower valency Bi^{3+} or Ca^{2+} into the CZ lattice, the reduction temperature was decreased and the OSC value was increased due to the formation of the oxygen vacancies for the ion migration. In the case of CZSn/Al_2O_3, the reduction temperature was lower and the OSC was higher than those of CZ/Al_2O_3 because the redox activity of the $Sn^{4+/2+}$ ions facilitated oxygen release and storage. Employing $Ni^{3+/2+}$ or $Fe^{3+/2+}$ as the dopant further lowered the reduction temperature and resulted in additional enhancement of the OSC value compared to the CZM/Al_2O_3 (M = Bi, Ca, Sn) samples.

Table 2.2 Reduction peak temperature and oxygen storage capacity of CZM/Al_2O_3 (M = Bi, Ca, Sn, Ni, Fe) and CZ/Al_2O_3 samples

Sample	Reduction temperature (°C)	OSC (μmol $O_2 \cdot g^{-1}$)
CZBi/Al_2O_3	425	140
CZCa/Al_2O_3	323	149
CZSn/Al_2O_3	306	112
CZNi/Al_2O_3	294	176
CZFe/Al_2O_3	284	195
CZ/Al_2O_3	498	76

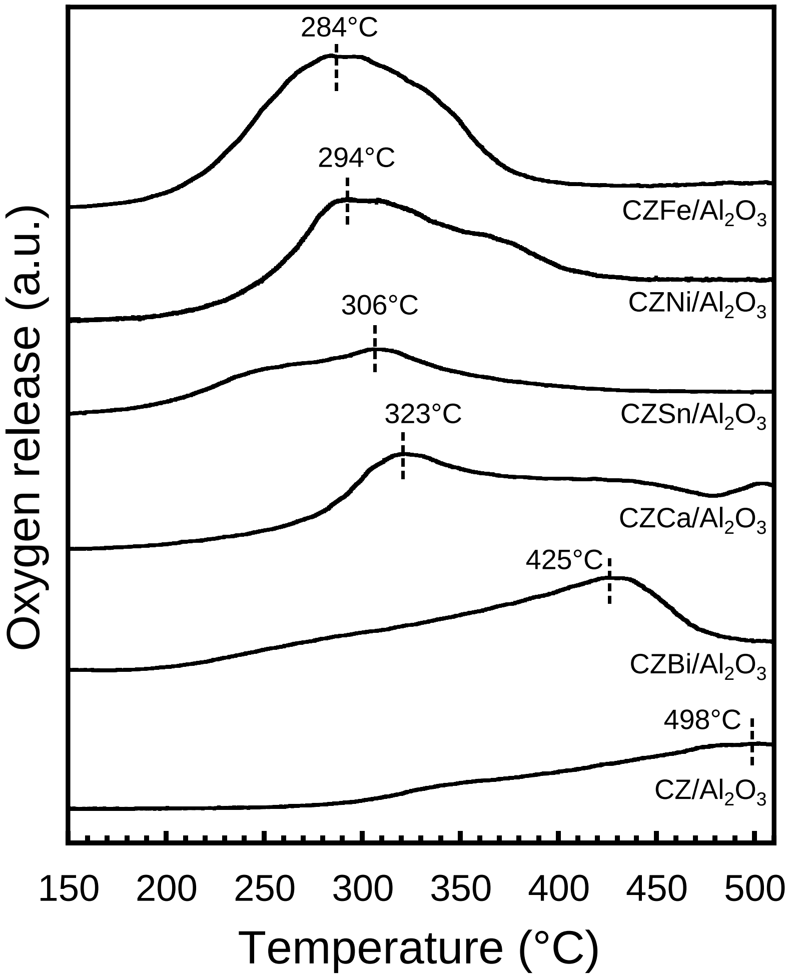

Figure 2.5. H_2-TPR profiles of the CZM/Al_2O_3 (M = Bi, Ca, Sn, Ni, Fe) and CZ/Al_2O_3 samples.

From the OSC value, amount of stored oxygen in the lattice (δ_{stored}) was estimated. The results are listed in Table 2.3 with the data of oxygen vacancy obtained (δ) by Rietveld analyses. Increases in the δ_{stored} value are seen to have increased the δ value, thus, it appears that oxygen storage capacity is related to the amount of oxygen vacancy for oxide-ion migration. The relationship between the oxide-ionic and electronic conductivities and the TPR and OSC results are further described in detail later in this chapter.

Table 2.3. Amount of stored oxygen (δ_{stored}) of CZM/Al_2O_3 (M = Bi, Ca, Sn, Ni, Fe) and CZ/Al_2O_3, and oxygen vacancy (δ) of CZM and CZ

Sample	Amount of stored oxygen (δ_{stored})	Oxygen vacancy (δ) in CZM and CZ
CZBi/Al_2O_3	0.0000102	0.158
CZCa/Al_2O_3	0.0000128	0.228
CZSn/Al_2O_3	0.0000089	0.134
CZNi/Al_2O_3	0.0000149	0.214
CZFe/Al_2O_3	0.0000165	0.232
CZ/Al_2O_3	0.0000067	0.084

The compositions and BET specific surface areas of the PdO-supported on CZM/Al_2O_3 (M = Bi, Ca, Sn, Ni, Fe) and CZ/Al_2O_3 catalysts are tabulated in Table 2.4. The compositions determined by XRF analysis were in good agreement with their stoichiometric values within the experimental error. The PdO/CZM/Al_2O_3 (M = Bi, Sn, Ni, Fe) catalysts showed lower surface areas than that of PdO/CZ/Al_2O_3 due to the lower melting point of Bi_2O_3 (817 °C) [28], SnO_2 (1630 °C) [29], NiO (1998 °C) [24], and Fe_2O_3 (1530 °C) [22] compared to CeO_2 (2445 °C) [23] and ZrO_2 (2710 °C) [23]. Here, the surface area of PdO/CZCa/Al_2O_3 was similar to that of PdO/CZ/Al_2O_3, since the melting point of CaO (2613 °C) [30] is similar value to those of CeO_2 and ZrO_2. From XRD measurements (Figure 2.6), the patterns clearly indicate the formation of a crystalline phase, indexed by the cubic fluorite-type structure, PdO phase, and γ-Al_2O_3 phase, while crystalline impurities were not observed.

Table 2.4. Measured compositions and surface areas of the PdO/CZM/Al_2O_3 (M = Bi, Ca, Sn, Ni, Fe) and PdO/CZ/Al_2O_3 catalysts

Catalyst	Measured composition	BET surface area ($m^2 \cdot g^{-1}$)
PdO/CZBi/Al_2O_3	11.3 wt% PdO / 16 wt% $Ce_{0.67}Zr_{0.18}Bi_{0.15}O_{2.0-\delta}$ / γ-Al_2O_3	195
PdO/CZCa/Al_2O_3	11.6wt%PdO / 16 wt%$Ce_{0.68}Zr_{0.17}Ca_{0.14}O_{2.0-\delta}$ / γ-Al_2O_3	220
PdO/CZSn/Al_2O_3	11.0wt%PdO / 16 wt%$Ce_{0.70}Zr_{0.19}Sn_{0.13}O_{2.0-\delta}$ / γ-Al_2O_3	208
PdO/CZNi/Al_2O_3	11.2wt%PdO / 16 wt%$Ce_{0.67}Zr_{0.18}Ni_{0.15}O_{2.0-\delta}$ / γ-Al_2O_3	184
PdO/CZFe/Al_2O_3	11.2 wt% PdO / 16 wt% $Ce_{0.67}Zr_{0.18}Fe_{0.15}O_{2.0-\delta}$ / γ-Al_2O_3	204
PdO/CZ/Al_2O_3	11.4 wt% PdO / 16 wt% $Ce_{0.81}Zr_{0.19}O_{2.0-\delta}$ / γ-Al_2O_3	225

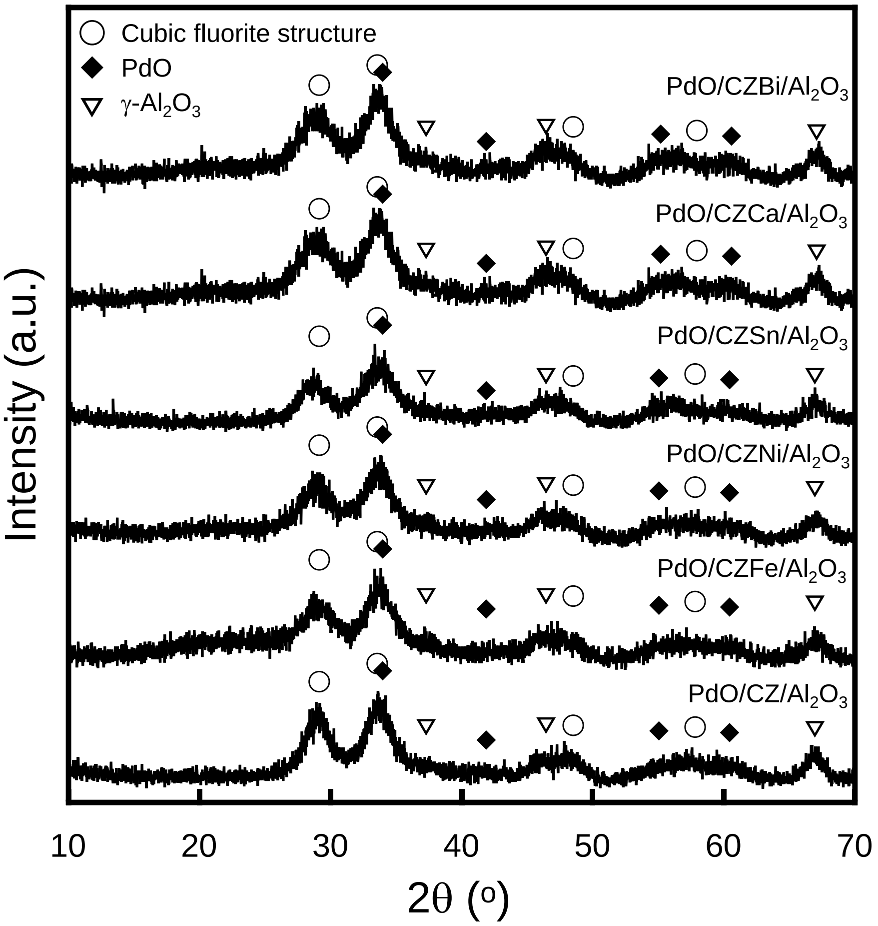

Figure 2.6. XRD patterns of PdO/CZM/Al_2O_3 (M = Bi, Ca, Sn, Ni, Fe) and PdO/CZ/Al_2O_3.

The PdO dispersions are tabulated in Table 2.5. The highest PdO dispersion was obtained for PdO/CZ/Al_2O_3. Figure 2.7 shows the XPS of the Pd 3d core-levels in the CZM and CZ samples. The XPS spectra of Pd 3d core-levels demonstrated that the oxidation state of the Pd species was confirmed as Pd^{2+} and Pd^0 for all samples prepared. The Pd^{2+} ratios in the Pd species are also summarized in Table 2.4. By introducing the dopant in the CZ lattice, the $Pd^{2+}/(Pd^{2+} + Pd^0)$ ratio was increased and the predominant Pd species was the divalent Pd^{2+} ion.

Table 2.5. PdO dispersions and $Pd^{2+}/(Pd^{2+} + Pd^0)$ ratios of the PdO/CZM/Al_2O_3 (M = Bi, Ca, Sn, Ni, Fe) and PdO/CZ/Al_2O_3 catalysts

Catalyst	PdO dispersion (%)	$Pd^{2+}/(Pd^{2+} + Pd^0)$ ratio (%)
PdO/CZBi/Al_2O_3	11.9	195
PdO/CZCa/Al_2O_3	9.7	220
PdO/CZSn/Al_2O_3	10.1	208
PdO/CZNi/Al_2O_3	11.2	184
PdO/CZFe/Al_2O_3	10.7	204
PdO/CZ/Al_2O_3	12.2	225

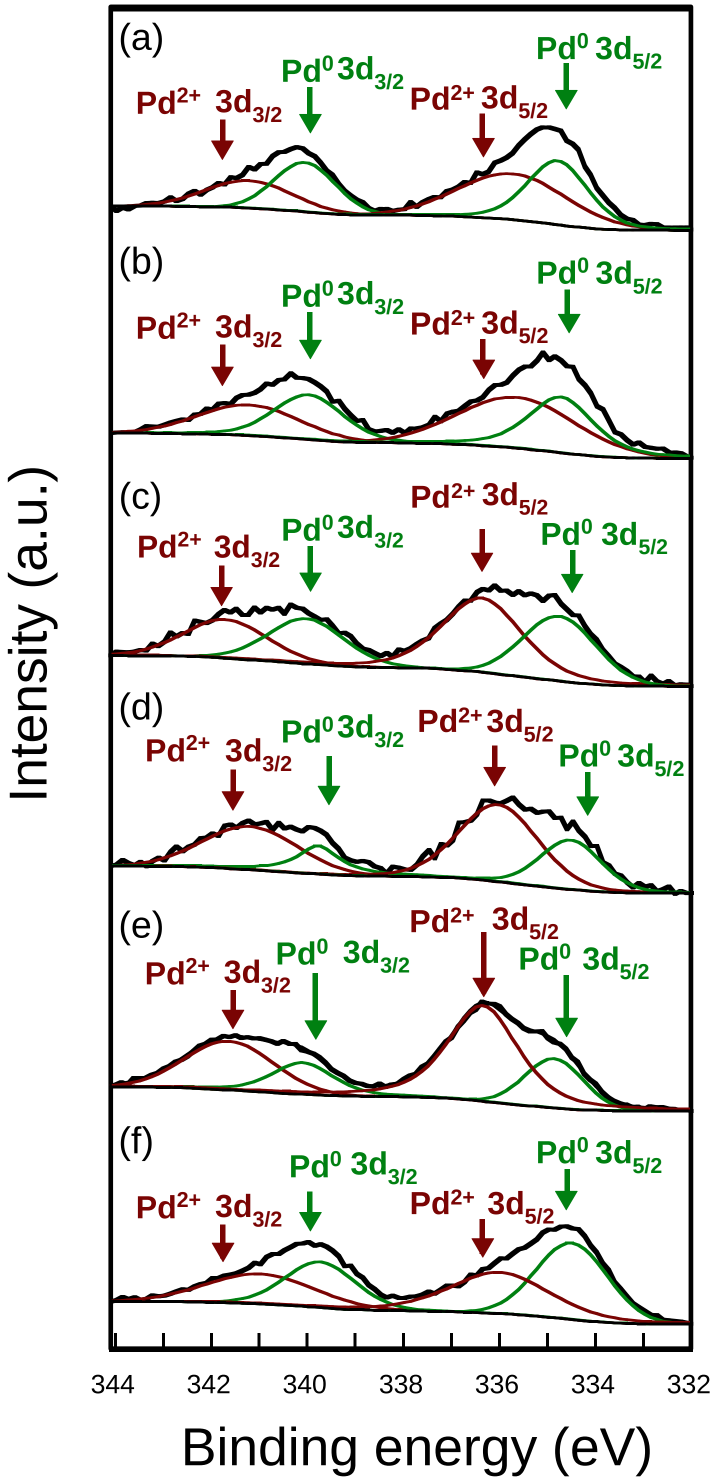

Figure 2.7. XPS spectra of Pd 3d core-levels of (a) PdO/CZBi/Al_2O_3, (b) PdO/CZCa/Al_2O_3, (c) PdO/CZSn/Al_2O_3, (d) PdO/CZNi/Al_2O_3, (e) PdO/CZFe/Al_2O_3, and (f) PdO/CZ/Al_2O_3.

Figure 2.8 shows the temperature dependencies of methane conversion over the PdO/CZM/Al_2O_3 (M = Bi, Ca, Sn, Ni, Fe) and PdO/CZ/Al_2O_3 catalysts. The catalytic activity was significantly improved by introducing Bi_2O_3, CaO, SnO_2, NiO, or Fe_2O_3 into the CZ lattice, although the surface areas and PdO dispersions of the PdO/CZM/Al_2O_3 samples were lower than those of the PdO/CZ/Al_2O_3. Regardless of the same dopant content, the PdO/CZNi/Al_2O_3 and PdO/CZFe/Al_2O_3 catalysts possessed higher activities compared to the PdO/CZBi/Al_2O_3, PdO/CZCa/Al_2O_3, and PdO/CZSn/Al_2O_3 cases. The effect of the promoters on the catalytic activity is discussed later in this chapter.

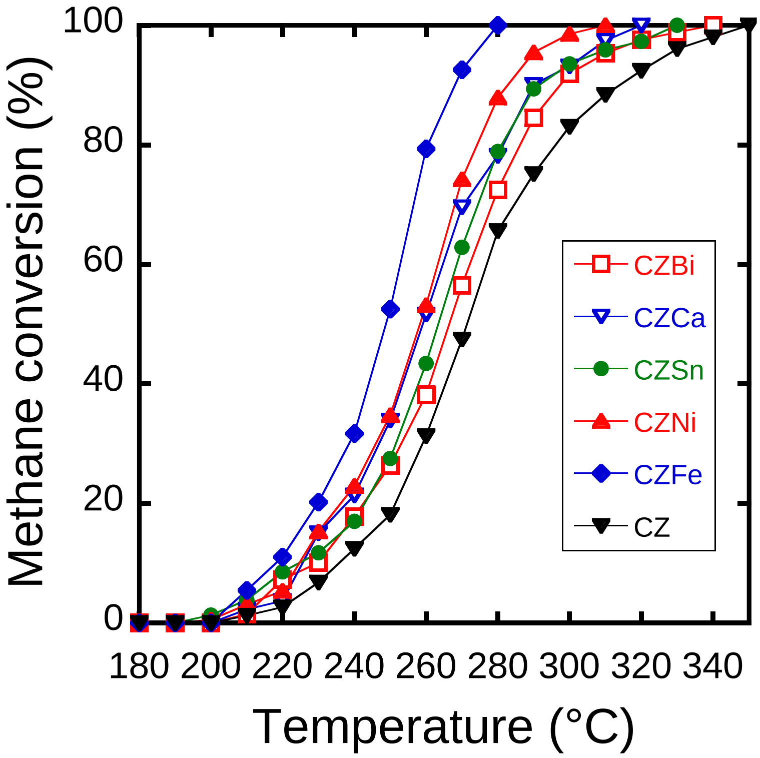

Figure 2.8. Temperature dependence of methane oxidation over the PdO/CZM/Al_2O_3 (M = Bi, Ca, Sn, Ni, Fe) and PdO/CZ/Al_2O_3 catalysts.

Figure 2.9 shows the resulting Arrhenius plots for methane conversion over the PdO/CZM/Al_2O_3 (M = Bi, Ca, Sn, Ni, Fe) and PdO/CZ/Al_2O_3 catalysts, and apparent activation energies for the catalysts are tabulated in Table 2.6. Here, apparent activation energy of the methane oxidation is estimated from the equations, as follows:

$$r = kC$$

$$k = A\exp(-E_\mathrm{a}/RT)$$

where r is the reaction rate, k is the rate constant, C is CH_4 concentration, A is the pre-exponential factor, E_a is the apparent activation energy, R is the gas constant, and T is the reaction temperature in K. The apparent activation energy can be obtained from the slope of the Arrhenius plot, in which ln k is plotted against the reciprocal temperature (Figure 2.9). Apparent activation energy was decreased with lowering the complete oxidation temperature, as listed in Table 2.6.

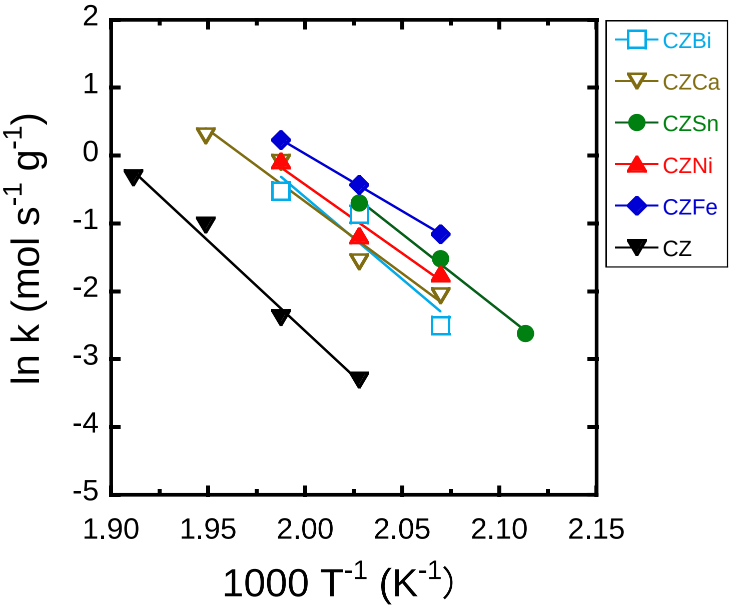

Figure 2.9. Arrhenius plots for methane conversion over the over the PdO/CZM/Al_2O_3 (M = Bi, Ca, Sn, Ni, Fe) and PdO/CZ/Al_2O_3 catalysts.

Table 2.6. Apparent activation energy (E_a) for methane conversion over the PdO/CZM/Al_2O_3 (M = Bi, Ca, Sn, Ni, Fe) and PdO/CZ/Al_2O_3 catalysts

Catalyst	Complete oxidation temperature (°C)	E_a (kJ·mol^{-1})
PdO/CZBi/Al_2O_3	340	201
PdO/CZCa/Al_2O_3	320	176
PdO/CZSn/Al_2O_3	330	187
PdO/CZNi/Al_2O_3	310	168
PdO/CZFe/Al_2O_3	280	140
PdO/CZ/Al_2O_3	350	221

Figure 2.10 shows the oxide-ionic and electronic conductivities (calculated from the AC conductivity and the ionic transference number at 500 °C) as functions of the oxygen occupancy. Increases in the oxygen vacancies evidently increased the oxide-ionic conductivity, as a result of the transport of oxide ions through these vacancies, such that the oxide-ionic conductivity was clearly dependent on the oxygen vacancy concentration. Furthermore, the electronic conductivities of the CZM (M = Sn, Ni, Fe) specimens were higher than those of the CZM (M = Bi, Ca) materials, indicating that the redox of $Sn^{4+/2+}$, $Ni^{3+/2+}$, and $Fe^{3+/2+}$ ions affected the increase of the electronic migration by accelerating the charge transfer owing to the valence changes of the dopant cations.

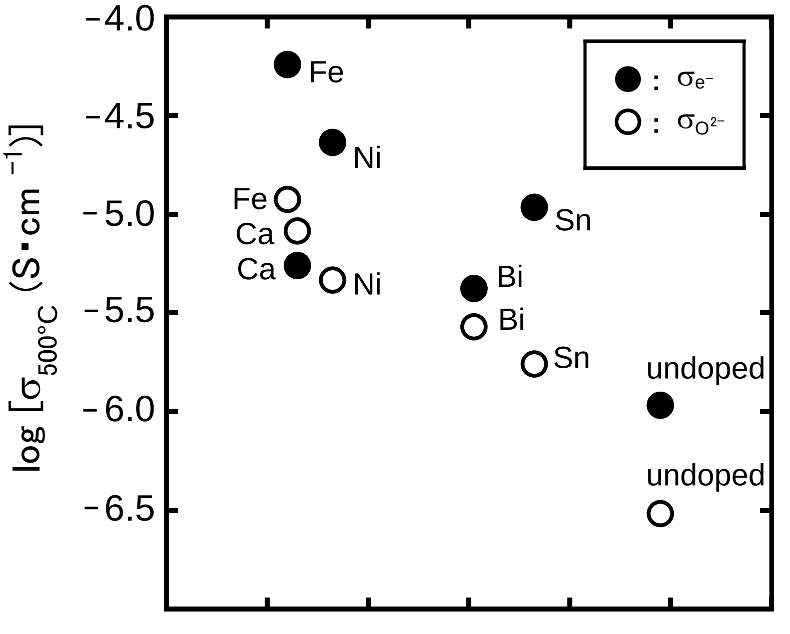

Figure 2.10. Relationships between the ionic and electronic conductivities at 500 °C and the oxygen occupancies of the CZM (M = Bi, Ca, Sn, Ni, Fe) and CZ solids.

Figure 2.11(a) shows the reduction temperatures of CZM/Al_2O_3 (M = Bi, Ca, Sn, Ni, Fe) and CZ/Al_2O_3 as functions of the oxide-ionic and electronic conductivities of the original CZM. Increases in the electronic conductivity are seen to have lowered the reduction temperature, indicating that the oxygen release of these samples is strongly affected by the electronic conductivity (that is, the redox characteristics) of the promoters. This effect is attributed to the correlation between oxygen release and the reduction of the component cations. Conversely, although the reduction temperature also decreased with increasing the oxide-ionic conductivity of CZ, CZBi and CZCa, the CZSn/Al_2O_3 and CZNi/Al_2O_3 reduction temperatures were significantly lower than that of CZCa/Al_2O_3 regardless of the lower oxide-ionic conductivities of CZSn and CZNi than the CZCa case. Therefore, the reduction temperature was predominantly influenced by the electronic conductivity compared to the oxide-ionic conductivity. Figure 2.11(b) shows the manner in which the OSC values of CZM/Al_2O_3 varied with the oxide-ionic and electronic conductivities of CZM. The OSC values substantially increased with increasing the ionic conductivity, indicating that the oxygen storage ability was affected by the oxide-ionic conductivity. This effect is attributed to the migration of the surface oxide ions toward the interior of the bulk material, where they combine with oxygen vacancies. In the case of CZCa/Al_2O_3, the OSC value was lower than that of CZNi/Al_2O_3, while CZCa showed higher oxide-ionic conductivity than CZNi. This phenomenon suggests that the OSC value was also affected by the electronic conductivity. This result can be elucidated by noting that the oxidative reactions of the constituent cations as well as the migration of oxide ions into the bulk material required electronic conduction to maintain the valency. In fact, the electronic conductivity of CZNi was higher than that of CZCa. Furthermore, increase of electronic conductivity raised the OSC values of all samples except for CZSn/Al_2O_3, for which the OSC value was lower than those of CZBi/Al_2O_3 and CZCa/Al_2O_3, because CZSn had lower oxide-ionic conductivity compared to CZBi and CZCa. Accordingly, both the oxide-ionic and electronic conductivities are crucial issues with regard to the OSC.

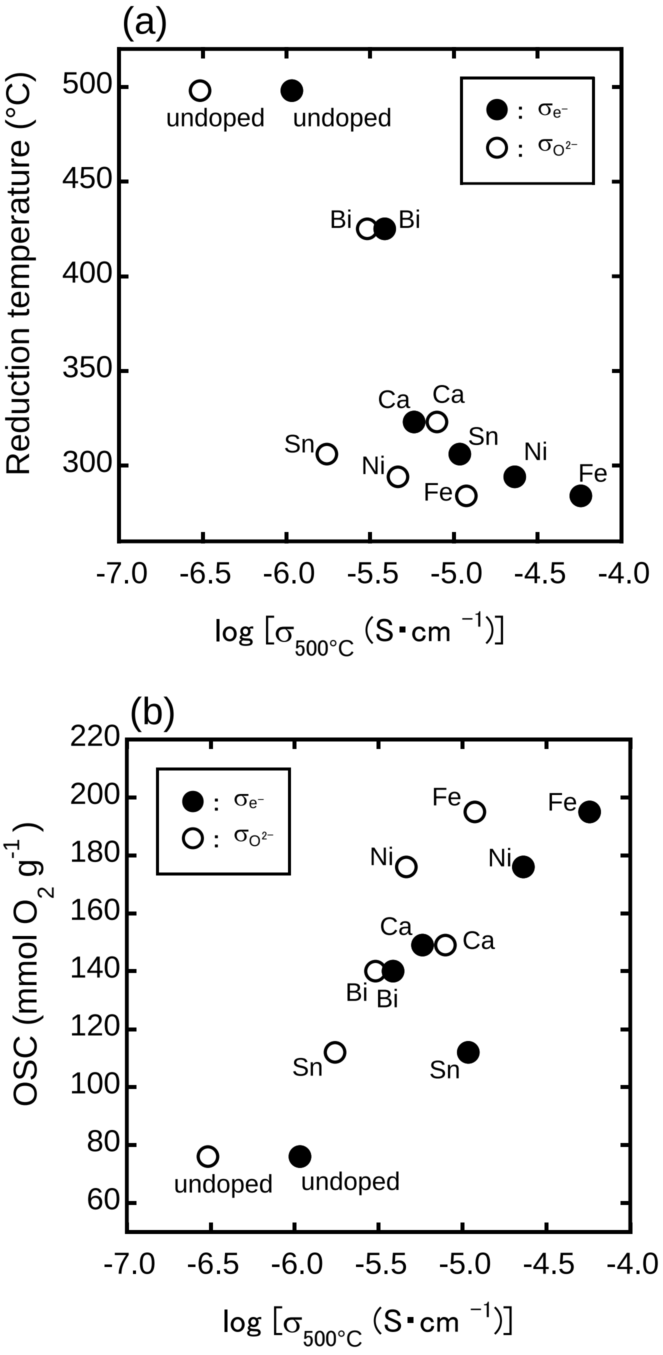

Figure 2.11. Dependencies of (a) the reduction temperatures and (b) the OSC of the CZM/Al_2O_3 (M = Bi, Ca, Sn, Ni, Fe) and CZ/Al_2O_3 samples on the oxide-ionic and electronic conductivities of the CZM and CZ promoters.

Figure 2.12 shows the dependence of the complete methane oxidation temperatures of the PdO/CZM/Al_2O_3 (M = Bi, Ca, Sn, Ni, Fe) catalysts on the reduction temperature and the OSC value of CZM/Al_2O_3 in order to investigate the effects of the oxygen release and storage abilities on the catalytic activity. As presented in Figure 2.12(a), lower reduction temperatures are related with lower complete oxidation temperatures, except for CZSn, indicating that the complete oxidation temperature was dependent on the reduction temperature (that is, on the oxygen release ability). This trend is attributed to acceleration of the active oxygen supply to the PdO activator for the methane oxidation. Here, it was confirmed that the Pd^{2+} amount was increased with lowering reduction temperature (Table 2.4). The PdO/CZSn/Al_2O_3 catalyst was found to require higher temperatures for complete oxidation compared to PdO/CZCa/Al_2O_3, while the reduction peak temperature of CZSn/Al_2O_3 was lower than that of CZCa/Al_2O_3, suggesting that the OSC value also affected catalytic activity. As a matter of fact, the OSC value of CZSn/Al_2O_3 was clearly lower than that of CZCa/Al_2O_3, as shown in Figure 2.12(b). This figure also indicates that increase of OSC values remarkably lowered the complete oxidation temperature. Thus, the oxygen storage ability is also significant with regard to the oxidation of methane, because the released oxygen has to be replenished by the absorption of gaseous oxygen. The complete oxidation temperature of PdO/CZBi/Al_2O_3 was higher than that of PdO/CZSn/Al_2O_3, despite the higher OSC value of CZBi/Al_2O_3 compared to CZSn/Al_2O_3. This result is attributed to the much higher reduction temperature required by CZBi/Al_2O_3 (Figure 2.12(a)). Accordingly, the catalytic activity was intimately related to the TPR and OSC results, and improvements in the catalytic activity were also affected by oxide-ionic and electronic conductivities of the CZM (M = Bi, Ca, Sn, Ni, Fe) promoters. Since the surface area and the PdO dispersion are not intimately related to the catalytic activity within the PdO series, it easily explains that the oxide-ionic and electronic conductivities of the promoter are important issues affecting the catalytic activity.

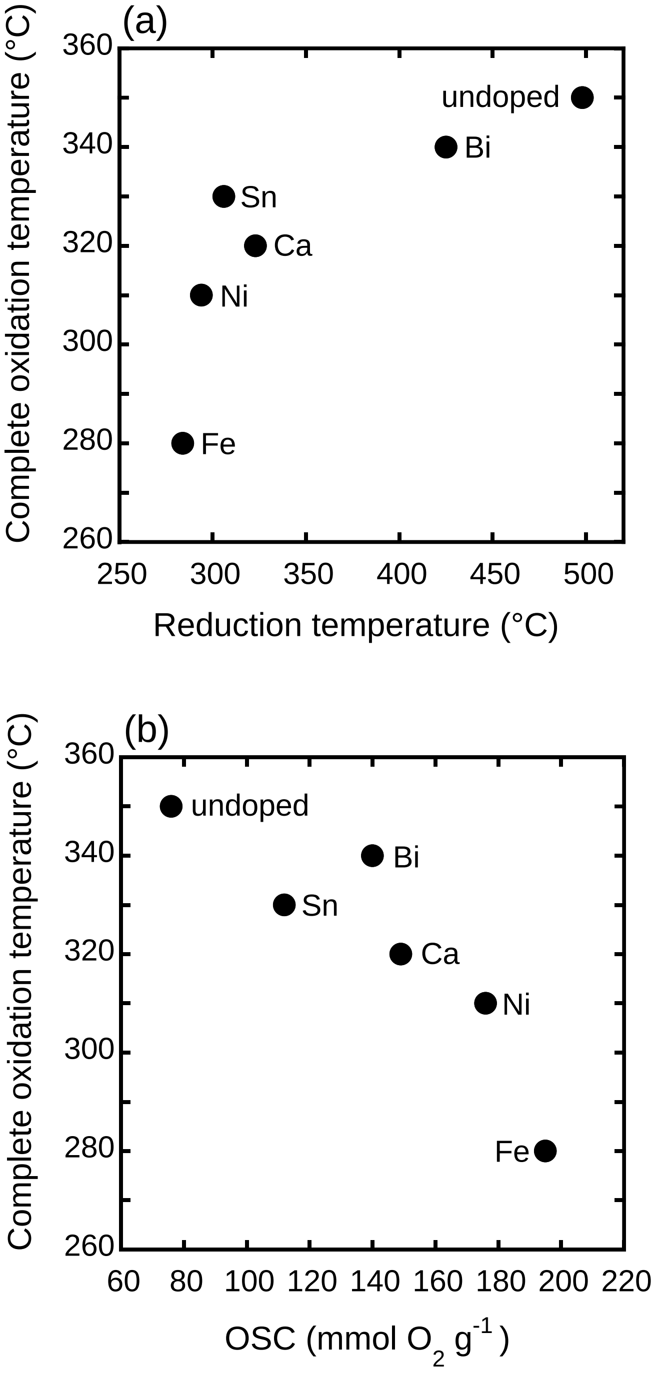

Figure 2.12. Dependencies of the complete oxidation temperatures of the PdO/CZM/Al_2O_3 (M = Bi, Ca, Sn, Ni, Fe) and PdO/CZ/Al_2O_3 catalysts on (a) the reduction temperatures and (b) the OSC values of the CZM/Al_2O_3 samples.

2.4 Conclusions

In this chapter, the relationships between conductivity, oxygen release and storage abilities, and catalytic activity for a series of the CeO_2–ZrO_2 based catalysts were investigated. The oxide-ionic conductivity of the CeO_2–ZrO_2–MO_x (M = Bi, Ca, Sn, Ni, Fe) promoters were increased with increasing the oxygen vacancy concentrations. Moreover, the electronic conductivity was clearly improved by introducing SnO_2, NiO, or Fe_2O_3, all of which possesses good redox properties owing to the $Sn^{4+/2+}$, $Ni^{3+/2+}$, and $Fe^{3+/2+}$ valence changes. The reduction temperatures of CeO_2–ZrO_2–MO_x/γ-Al_2O_3 (M = Bi, Ca, Sn, Ni, Fe) obtained from hydrogen temperature-programmed reduction analysis were principally dependent on the electronic conductivity rather than the oxide-ionic conductivity of the promoter. In contrast, oxygen storage capacity was affected by both the oxide-ionic and electronic conducting properties. The catalytic activities during methane oxidation of materials composed of PdO supported on CeO_2–ZrO_2–MO_x/γ-Al_2O_3 (M = Bi, Ca, Sn, Ni, Fe) were intimately related to the oxygen release and storage abilities rather than on the surface area. Accordingly, it is revealed that the oxide-ionic and electronic conductivities of the promoter obviously affect the catalytic methane oxidation activity of the catalyst.

Chapter 3

Complete Combustion of Toluene using Novel CeO_2–ZrO_2 Based Catalysts

3.1 Introduction

In chapter 1, it was demonstrated the CeO_2–ZrO_2–MO_x (M = Fe, Ni) promoters possessed the high oxygen release and storage abilities, and the complete methane oxidations were realized at 280 °C and 300 °C for PdO supported on CeO_2–ZrO_2–MO_x (M = Fe, Ni), respectively.

In this chapter, in order to remove toluene (C_7H_8) which is urgently required for removal from the atmosphere at temperature as low as possible, I synthesized catalysts by the combination of Pt with a high catalytic oxidation activity, CeO_2–ZrO_2–NiO as a promoter, and γ-Al_2O_3 as a support, and the catalytic activities of Pt/CeO_2–ZrO_2–NiO/γ-Al_2O_3 for toluene oxidation were investigated.

3.2 Experimental Procedure

The $Ce_{0.64}Zr_{0.16}Ni_{0.2}O_{2.0-\delta}$/$\gamma$-$Al_2O_3$ (CZNi/Al_2O_3) samples were synthesized via the conventional wet coprecipitation method. Aqueous solutions of 1.0 mol·L^{-1} $Ce(NO_3)_3$, 0.1 mol·L^{-1} $ZrO(NO_3)_2$, and 0.1 mol·L^{-1} $Ni(NO_3)_2$ were mixed with 15 mL of 3 mol·L^{-1} HNO_3 in stoichiometric amounts, and then, the solution was impregnated on the pulverized γ-Al_2O_3 powder. The pH of the solution was adjusted to 11 by the dropwise addition of aqueous ammonia (6%), and stirred at room temperature. The resulting precipitate was collected by filtration, and calcined at 500 °C for 1 h under the air atmosphere. Supported platinum catalysts (Pt/CZNi/Al_2O_3) were prepared by the impregnation of platinum colloid stabilized with PVP (Tanaka Kikinzoku Kogyo) into the CZNi/Al_2O_3 samples. Subsequently, the catalysts were calcined at 500 °C for 4 h. The amounts of Pt and CZNi were adjusted in the range of 7.0–12wt% and 10–25wt%, respectively.

X-ray fluorescence analysis (XRF; ZSX100e, Rigaku) was measured to confirm the compositions of the catalysts. X-ray powder diffraction (XRD; SmartLab, Rigaku) measurements were measured with Cu-Kα radiation (40 kV, 30 mA). Brunauer-Emmett-Teller (BET) specific surface area was measured by nitrogen adsorption at −196 °C (TriStar 3000, Shimadzu). Temperature programmed reduction (TPR) measurement was measured under a flow of 5 vol% hydrogen-argon (50 $\mathrm{mL{\cdot}min^{-1}}$) up to 500 °C, and then, the oxygen storage capacity (OSC) was carried out using the pulse-injection method at 427 °C.

The toluene oxidation was carried out using a conventional fixed-bed flow reactor with a 10 mm diameter quartz glass tube by feeding a gas mixture of toluene (900 ppm) and air (balance) at a rate of 20 $\mathrm{mL{\cdot}min^{-1}}$ over 0.1 g of catalyst, i.e., the space velocity was 12,000 $\mathrm{L{\cdot}kg^{-1}{\cdot}h^{-1}}$. The catalytic activity was evaluated in terms of the approximately-constant toluene conversion at each temperature maintained for over half an hour. The gas composition was analysed using gas chromatograph with a flame ionization detector (FID; Shimadzu GC-8AIF). For the water durability test of catalyst, the toluene oxidation was performed by using wet toluene-air gas (0.6 and 3.1vol% H_2O) which were obtained by passing into 0 and 25 °C water, respectively.

3.3 Results and Discussion

The compositions and BET specific surface areas of the 10wt%Pt/(10–25)wt%CZNi/Al_2O_3 catalysts are tabulated in Table 3.1. For theses samples, the compositions determined by XRF analysis were in good agreement with the expected stoichiometric values within the experimental error.

Table 3.1. Measured compositions and BET surface areas of 10wt%Pt/(10–25)wt%CZNi/Al_2O_3

Catalyst	Measured composition	BET surface area ($m^2 \cdot g^{-1}$)
10wt%Pt /25wt%CZNi/Al_2O_3	10.6wt%Pt/ 26wt%$Ce_{0.65}Zr_{0.16}Ni_{0.19}O_{2.0-\delta}$/γ-$Al_2O_3$	145
10wt%Pt /20wt%CZNi/Al_2O_3	11.2wt%Pt/ 20wt%$Ce_{0.66}Zr_{0.16}Ni_{0.18}O_{2.0-\delta}$/γ-$Al_2O_3$	151
10wt%Pt /16wt%CZNi/Al_2O_3	10.4wt%Pt/ 16wt%$Ce_{0.67}Zr_{0.15}Ni_{0.18}O_{2.0-\delta}$/γ-$Al_2O_3$	162
10wt%Pt /10wt%CZNi/Al_2O_3	11.0wt%Pt/ 10wt%$Ce_{0.66}Zr_{0.16}Ni_{0.18}O_{2.0-\delta}$/γ-$Al_2O_3$	173

Figure 3.1 shows the temperature dependences for methane conversion over the 10wt%Pt/(10–25)wt%CZNi/Al_2O_3 catalysts. The highest activity was obtained for the 10wt%Pt/16wt%CZNi/Al_2O_3 catalysts, and complete oxidation of toluene was realized at 100 °C. Therefore, the optimum amount of CZNi was determined to be 16wt%.

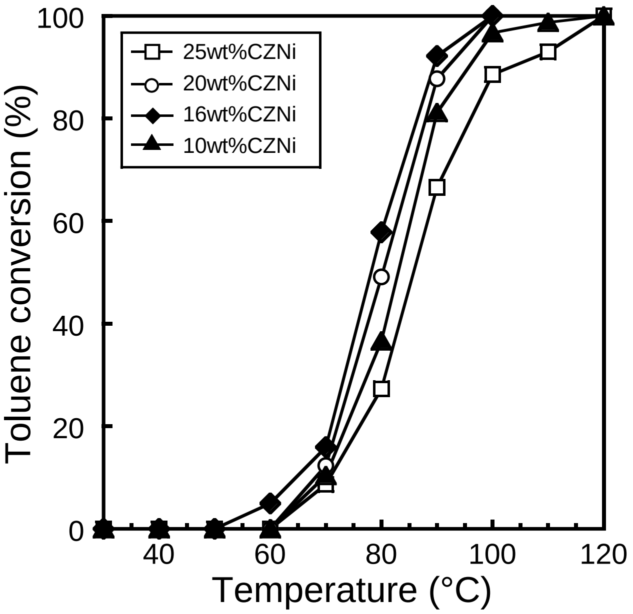

Figure 3.1. Temperature dependencies of the oxidation activities of the 10wt%Pt/(10–25) wt%CZNi/Al_2O_3.

Figure 3.2 shows the temperature dependences for toluene conversion over the (7–12)wt%Pt/16wt%CZNi/Al_2O_3 catalysts. For comparison, the data of 10wt%Pt/16wt%CZ/Al_2O_3 is also presented. Among the (7–12)wt%Pt/CZNi/Al_2O_3 catalysts, the highest activity was confirmed for 10wt%Pt/CZNi/Al_2O_3. For 10wt%Pt/16wt%CZNi/Al_2O_3, toluene conversion began at 60 °C, and complete toluene oxidation was realized at the temperature as low as 100 °C. This combustion temperature value is 40 °C lower than that for 10wt%Pt/16wt%CZ/Al_2O_3 (140 °C), regardless of the low surface area of 10wt%Pt/16wt%CZNi/Al_2O_3 (162 $m^2 \cdot g^{-1}$) compared to the 10wt%Pt/16wt%CZ/Al_2O_3 case (183 $m^2 \cdot g^{-1}$). This improvement of the catalytic activity is affected by the increase of oxygen release and storage abilities due to the generation of oxygen vacancy and the redox property of $Ni^{3+/2+}$ by doping NiO into CeO_2–ZrO_2. In addition, the complete oxidation temperature for 10wt%Pt/CZNi/Al_2O_3 was also lower than those for Pt/CeO_2–ZrO_2–Bi_2O_3/Al_2O_3 (120 °C) [31] and Pt/CeO_2–ZrO_2–SnO_2/Al_2O_3 (110 °C) [32], reported previously.

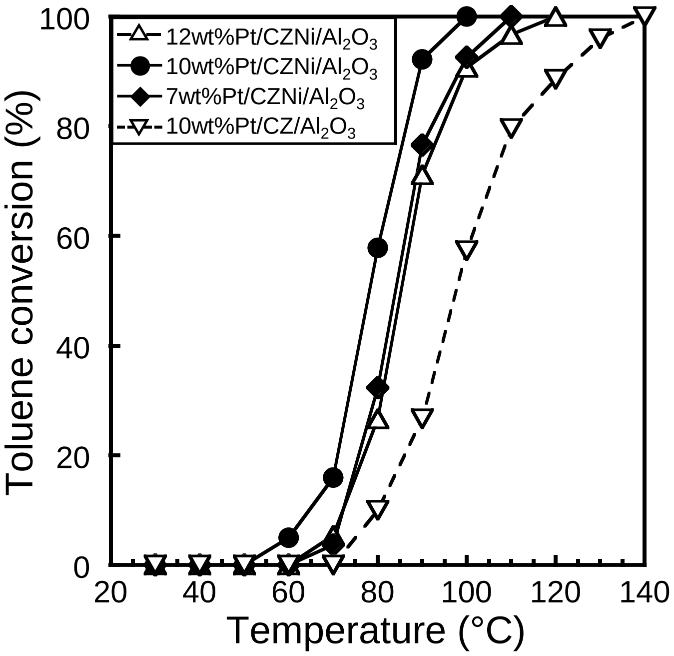

Figure 3.2. Temperature dependencies of toluene oxidation over the (7–12)wt%Pt/16wt%CZNi /Al_2O_3 and 10wt%Pt/16wt%CZ/Al_2O_3 catalysts.

In order to investigate the oxygen release properties, TPR measurements were carried out. Figure 3.3 shows the results for the 10wt%Pt/16wt%CZNi/Al_2O_3 and 10wt%Pt/16wt%CZ/Al_2O_3 catalysts. In the case of 10wt%Pt/16wt%CZNi/Al_2O_3, the peak was observed at 92 °C, attributed to the reduction of oxidized platinum species [33,34]. To compare with 10wt%Pt/16wt%CZ/Al_2O_3, a shift of the peak to lower temperatures and an increase of the peak intensity were recognized. This result indicates that the active oxygen species were effectively supplied to the platinum activator from the CeO_2–ZrO_2–NiO promoter.

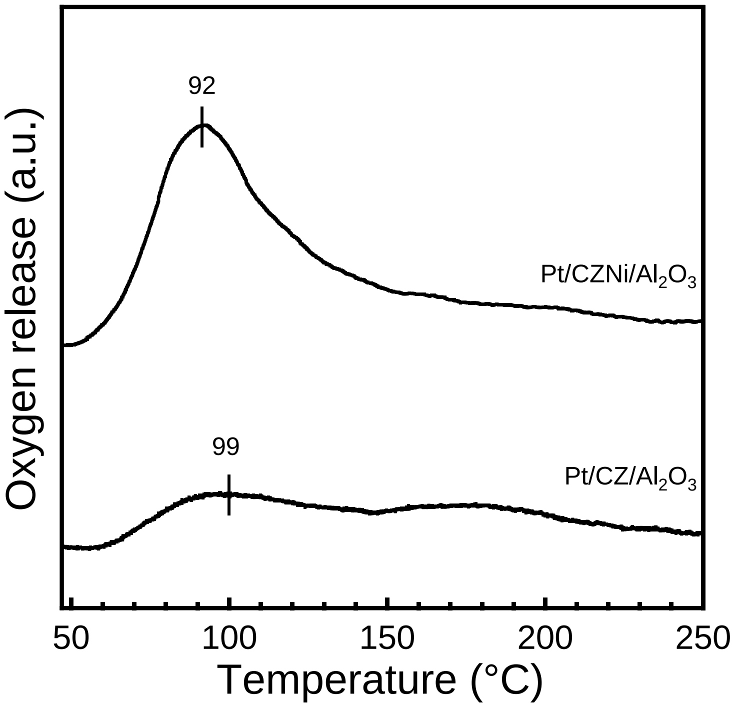

Figure 3.3. H_2-TPR profiles of 10wt%Pt/16wt%CZNi/Al_2O_3 and 10wt%Pt/16wt%CZ/Al_2O_3.

For the practical usage of the toluene oxidation catalyst, water vaper, generated by toluene combustion and contained in the atmosphere air, usually acts as a catalytic poisoning caused by the competition of water molecules with toluene molecules for adsorption on the activities of the catalyst. Figure 3.4 shows the catalytic activity using 10wt%Pt/16wt%CZNi/Al_2O_3, carried out under dry, 0.6 vol% H_2O, and then, 3.1 vol% H_2O conditions. Since the activity was maintained, under the moist conditions, it is clear that 10wt%Pt/16wt%CZNi/Al_2O_3 possesses high water durability. In addition, the activity was investigated continuously without annealing after each examination, indicating that the deactivation by coking was not confirmed.

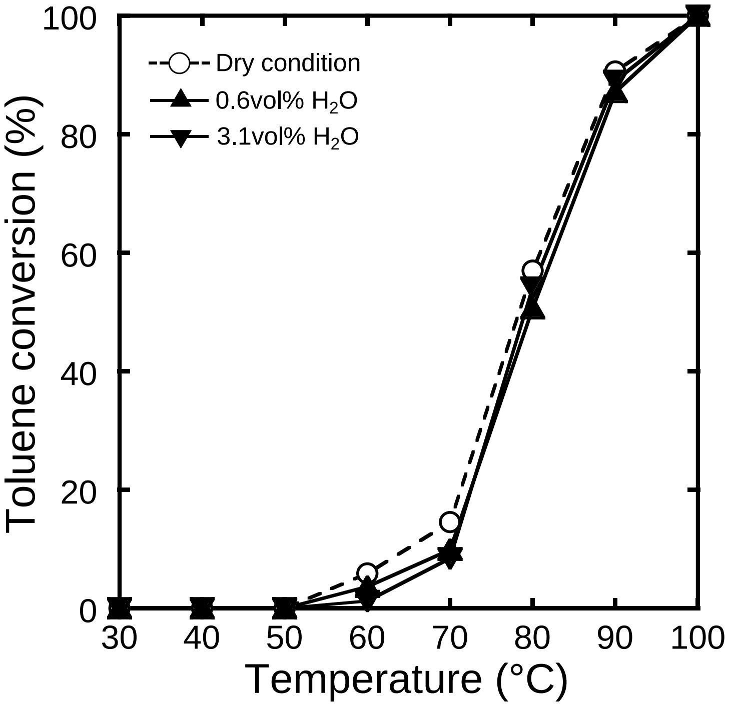

Figure 3.4. Temperature dependencies of toluene combustion on 10wt%Pt/16wt%CZNi/Al_2O_3 in moist (0.6 and 3.1vol% H_2O) and dry conditions.

3.4 Conclusions

In this chapter, for toluene complete oxidation at moderate temperatures, Pt/CeO_2–ZrO_2–NiO/γ-Al_2O_3 catalysts were synthesized via coprecipitation and impregnation methods. The enhancement of the oxygen release and storage abilities of the CeO_2–ZrO_2–NiO as a promoter is attributed to the formation of oxygen vacancy and the redox of $Ni^{3+/2+}$ ions. 10wt%Pt/16wt%$Ce_{0.64}Zr_{0.16}Ni_{0.2}O_{2.0-\delta}$/γ-$Al_2O_3$ catalyst possessed the highest catalytic activity, and toluene was completely oxidized at the temperature as low as 100 °C.

Summary

In the study of this thesis, the development of novel catalysts that can realize completely combustion of methane and toluene at moderate temperatures.

The results obtained through this work are summarized as follows:

Chapter 1

For methane complete oxidation at moderate temperatures, Fe_2O_3 and NiO were introduced into the CeO_2–ZrO_2 lattice to increase the oxygen release and storage abilities. The introduction of Fe_2O_3 and NiO into the CeO_2–ZrO_2 lattice was found to effectively enhance the oxygen release and storage abilities due to the formation of oxygen vacancies and the redox of $Fe^{3+/2+}$ or $Ni^{3+/2+}$ ions. The 11.3wt%PdO/16wt%$Ce_{0.68}Zr_{0.17}Fe_{0.15}O_{2.0-\delta}$/γ-$Al_2O_3$ and 11.3wt%PdO/20wt%$Ce_{0.64}Zr_{0.16}Ni_{0.2}O_{2.0-\delta}$/γ-$Al_2O_3$ catalysts were found to achieve the complete methane oxidation at the temperatures as low as 280 °C and 300 °C, respectively.

Chapter 2

The relationships between conductivity, oxygen release and storage abilities, and catalytic activity for a series of CeO_2–ZrO_2 based catalysts were investigated. The oxide-ionic conductivity of the CeO_2–ZrO_2–MO_x (M = Bi, Ca, Sn, Ni, Fe) promoters was increased with increasing the oxygen vacancy concentrations. Moreover, the electronic conductivity was clearly improved by introducing SnO_2, NiO or Fe_2O_3, all of which possesses good redox properties owing to the $Sn^{4+/2+}$, $Ni^{3+/2+}$ and $Fe^{3+/2+}$ valence changes. The reduction temperatures of the CeO_2–ZrO_2–MO_x/γ-Al_2O_3 samples obtained from hydrogen temperature-programmed reduction analysis were principally dependent on the electronic conductivity rather than the oxide-ionic conductivity of the promoter. In addition, oxygen storage capacity was affected by both the oxide-ionic and electronic conducting properties. The catalytic activities during methane oxidation of the catalysts composed of PdO supported on CeO_2–ZrO_2–MO_x/γ-Al_2O_3 were affected by the oxygen release and storage abilities rather than on the surface area. Accordingly, it is revealed that the oxide-ionic and electronic conductivities of the promoter obviously affect the catalytic methane oxidation activity of the catalyst.

Chapter 3

For toluene complete oxidation at moderate temperatures, Pt/CeO_2–ZrO_2–NiO/γ-Al_2O_3 catalysts were prepared. The highest activity for the toluene combustion was obtained for the 10wt%Pt/16wt%$Ce_{0.64}Zr_{0.16}Ni_{0.2}O_{2.0-\delta}$/γ-$Al_2O_3$ catalyst, and the toluene was completely oxidized at the temperature as low as 100 °C.

References

[1] J. Pérez-Ramírez, *Appl. Catal. B: Environ.*, **70**, 31 (2007).

[2] Y. Li, J.N. Armor, *Appl. Catal. B: Environ.*, **3**, 275 (1994).

[3] H. Knöppel, H. Schauenburg, *Environ. Int.*, **15**, 413 (1989).

[4] H.B. Elkins, G.W. McCarl, H.G. Brugsch, J.P. Fahy, *Am. Ind. Hyg. Assoc. J.*, **23**, 265 (1962).

[5] V. Decottignies, L. Gasnot, J.F. Pauwels, *Combust. Flame*, **130**, 225 (2002).

[6] A.G. Merzhanov, *Combustion Process in Chemical Technology and Metallurgy*, 1 (1975).

[7] H. Zaitan, D. Bianchi, O. Achak, T. Chafik, *J. Hazard. Mater.*, **153**, 852 (2008).

[8] J.J. Spivey, *Ind. Eng. Chem. Res.*, **26**, 2165 (1987).

[9] Y. Nakaya, T. Sakurai, in *Handbook of Environmental Catalyst*, NTS Publishers, Tokyo, 626 (2001).

[10] R.J. Farrauto, M.C. Hobson, T. Kennelly, E.M. Waterman, *Appl. Catal. A: Gen.*, **81**, 227 (1992).

[11] A. O'malley, B.K. Hodnett, *Catal. Today*, **54**, 31 (1999).

[12] C. Force, E. Roman, J.M. Guil, J. Sanz, *Langmuir*, **23**, 4569 (2007).

[13] T. Montini, M. Melchionna, M. Monai, P. Fornasiero, *Chem. Rev.*, **116**, 5987 (2016).

[14] C.E. Hori, H. Permana, K.S. Ng, A. Brenner, K. More, K.M. Rahmoeller, D. Belton, *Appl. Catal. B: Environ.*, **16**, 105 (1998).

[15] C. Bozo, N. Guilhaume, J.M. Herrmann, *J. Catal.*, **203**, 393 (2001).

[16] K. Yasuda, A. Yoshimura, A. Katsuma, T. Masui, N. Imanaka, *Bull. Chem. Soc. Jpn.*, **85**, 522 (2012).

[17] N. Imanaka, T. Masui, K. Minami, K. Koyabu, *Chem. Mater.*, **17**, 6511 (2005).

[18] K. Minami, T. Masui, N. Imanaka, L. Dai B. Pacaud, *J. Alloys Compd.*, **408**, 1132 (2006).

[19] T. Masui, K. Minami, K. Koyabu, N. Imanaka, *Catal. Today*, **117**, 187 (2006).

[20] N. Imanaka, T. Masui, K. Minami, K. Koyabu, T. Egawa, *Adv. Mater.*, **19**, 1608 (2007).

[21] K. Yasuda, T. Masui, T. Miyamoto, N. Imanaka, *J. Mater. Sci.*, **46**, 4046 (2011).

[22] P.M. Rao, X. Zheng, *Nano Lett.*, **9**, 3001 (2009).

[23] P. Duran, M. Gonzalez, C. Moure, J.R. Jurado, C. Pascual, *J. Mater. Sci.*, **25**, 5001 (1990).

[24] S.L. Che, K. Takada, K. Takashima, O. Sakurai, K. Shinozaki, N. Mizutani, *J. Mater. Sci.*, **34**, 1313 (1999).

[25] F. Izumi, K. Momma, *Solid State Phenom.*, **130**, 15 (2007).

[26] R.D. Shannon, *Acta Crystallogr., Sect. A*, **32**, 751 (1976)

[27] W. Shan, M. Luo, P. Ying, W. Shen, C. Li, *Appl. Catal. A*: *Gen.*, **246**, 1 (2003).

[28] Y.S. Cho, V.L. Burdick, V.R. Amarakoon, *J. Am. Ceram. Soc.*, **82**, 1416 (1999).

[29] P.E.D. Morgan, R.M. Housley, *J. Am. Ceram. Soc.*, **78**, 263 (1995).

[30] W.M. Haynes, M. William, *CRC handbook of chemistry and physics (92nd ed.)*, **2011**, 4 FL: CRC press, Boca raton.

[31] T. Masui, H. Imadzu, N. Matsuyama, N. Imanaka, *J. Hazard. Mater.*, **176**, 1106 (2010).

[32] K. Yasuda, A. Yoshimura, A. Katsuma, T. Masui, N. Imanaka, *Bull. Chem. Soc. Jpn.*, **85**, 522 (2012).

[33] D.W. Jeong, W.J. Jang, J.O. Shim, W.B. Han, H.M. Kim, Y.L. Lee, J.W. Bae, H.S. Roh, *Renew. Energy*, **79**, 78 (2015).

[34] Y.D. Bi, W. Zhang, H.Y. Xu, W.Z. Li, *Catal. Lett.*, **119**, 126 (2007).

Acknowledgements

The author would like to express his heartfelt gratitude to Professor Dr. Nobuhito Imanaka, Divison of Applied Chemistry, Graduate School of Engineering, Osaka University, for his continuous guidance, many invaluable suggestions, and science encouragement throughout the work. The author is very grateful to Dr. Naoyoshi Nunotani, Divison of Applied Chemistry, Graduate School of Engineering, Osaka University, for his continuous guidance and stimulating discussions for carrying out this work. The author is also indebted to Dr. Shinji Tamura, Divison of Applied Chemistry, Graduate School of Engineering, Osaka University, for his helpful suggestions and apposite advice.

The author is deeply grateful to Professor Dr. Ken-ichi Machida, Divison of Applied Chemistry, Graduate School of Engineering, Osaka University, and Professor Dr. Masaya Nogi, the Institute of Scientific and Industrial Research (Divison of Applied Chemistry, Graduate School of Engineering), Osaka University, for reviewing this thesis and giving their valuable comments.

Special thanks should be given to author's co-workers, Mr. Changmin Cho, Mr. Ryoshuke Nagai, Mr. Naoki Moriyama, Mr. Abdul Rohman Supandi, Mr. Muhammad Radzi Iqbal, Mr. Yoshiki Asakawa, Mr. Kenji Matsuo, Mr. Shohei Saeki, and Mr. Masanari Takashima for their helpful assistance and support in the course of this work, and the other members of the research group under direction of Pro fessor Dr. Nobuhito Imanaka, Osaka University.

The author would like to thank to Professor Dr. Dong Sik Bae of Changwon National Universitiy in South Korea for his helpful comments and encouragement.

The Rotary Yoneyama Memorial Foundation is also acknowledged for financial support.

Finally, the author would like to extend deep gratitude to his parents, Mr. Changseok Jeong and Ms. Sunhee Kim, his sister, Ms. Jieun Jeong, and all members of his family for their encouragement, continuous understanding, and perpetual supports.